

## CHARACTERIZING THE LOW-REDSHIFT INTERGALACTIC MEDIUM TOWARDS PKS1302-102

KATHY L. COOKSEY<sup>1</sup>, JASON X. PROCHASKA<sup>2</sup>, HSIAO-WEN CHEN<sup>3</sup>, JOHN S. MULCHAEY<sup>4</sup>, AND BENJAMIN J. WEINER<sup>5</sup>

*Draft 1: June 12, 2007*

### ABSTRACT

We present a detailed analysis of the intergalactic metal-line absorption systems in the archival *HST*/STIS and *FUSE* ultraviolet spectra of the low-redshift quasar PKS1302-102 ( $z_{QSO} = 0.2784$ ). We supplement the archive data with CLOUDY ionization models and a survey of galaxies in the quasar field. There are 23 strong Ly $\alpha$  absorbers with column densities  $\log N_{\text{HI}} > 14$ . Of these, six are associated with at least C III  $\lambda 977$  absorption ( $\log N(\text{C}^{++}) > 13$ ); this implies a redshift density  $dN_{\text{CIII}}/dz = 33^{+11}_{-8}$  (68% confidence limits) for lines with rest equivalent width  $W_r > 30$  mÅ. Two systems show O VI  $\lambda\lambda 1031, 1037$  absorption in addition to C III ( $\log N(\text{O}^{+5}) > 14$ ). One is a partial Lyman limit system ( $\log N_{\text{HI}} = 17$ ) with associated C III, O VI, and Si III  $\lambda 1206$  absorption. There is a tentative third O VI system that does not have C III detected. For three O VI detections,  $dN_{\text{OVI}}/dz = 15^{+8}_{-5}$  for  $W_r > 30$  mÅ. We also search for O VI doublets without Ly $\alpha$  absorption but identify none. From CLOUDY modeling, these metal-line systems have metallicities spanning the range  $-3 \lesssim [M/H] \lesssim -0.5$ . All of the detected O VI absorbers can be described well by collisional ionization models. However, the two O VI systems with associated C III absorption cannot be single-phase, collisionally-ionized media based on the relative abundances of the metals and kinematic arguments. From the galaxy survey, we discover that the absorption systems are in a diverse set of galactic environments. Each metal-line system has two to ten galaxies within  $500 \text{ km s}^{-1}$  and  $600 h_{75}^{-1} \text{ kpc}$  with  $L > 0.1L_*$ .  
*Subject headings:* IGM : metals, O VI, galaxies—techniques : UV spectroscopy

### 1. INTRODUCTION

The baryonic content of the Universe is well constrained by Big Bang nucleosynthesis models, the cosmic microwave background, and the high-redshift Lyman- $\alpha$  forest (*e.g.*, O’Meara et al. 2006; Spergel et al. 2006). However, surveys of the nearby Universe reveal a dearth of baryons in stars, galaxies, and clusters (Fukugita & Peebles 2004). Recent cosmological simulations have placed the most likely reservoir of baryons at low redshift in moderately overdense, collisionally ionized gas, called the warm-hot intergalactic medium (WHIM; Davé et al. 2001; Fang & Bryan 2001; Cen et al. 2001). With temperatures in the range  $10^5$ – $10^7$  K, the most sensitive tracer with current observational facilities is the O VI doublet  $\lambda\lambda 1031, 1037$  Å, which dominates collisionally ionized gas at  $T \approx 3 \times 10^5$  K, as discussed below.

The O VI doublet is a valuable absorption feature observationally because it has a characteristic separation and rest equivalent width ( $W_r$ ) ratio for unsaturated features (2 : 1 for the  $\lambda 1031.93$  :  $\lambda 1037.62$  pair). Furthermore, Oxygen is the most abundant metal and the O<sup>+5</sup> ion is an effective tracer of the low temperature WHIM (Tripp et al. 2006b). Assuming collisional ionization equilibrium, other ion species (*e.g.* O VIII, Mg X, Ne VIII) have greater abundances in the higher WHIM temperature range, where it is predicted there are more

baryons; however, these other ions are extremely difficult to detect at low redshifts. Current X-ray telescopes are not up to the task but for a few systems (Wang et al. 2005; Williams et al. 2006; Nicastro et al. 2005).

Cosmological simulations make four important predictions about the content, temperature, ionization mechanism, and density of the WHIM. The WHIM contains  $\sim 40\%$  of the baryons in the low-redshift Universe (Davé et al. 2001; Cen et al. 2001). It has characteristic overdensity  $10 \lesssim \delta \lesssim 30$  and is shock heated to  $T \approx 10^5$ – $10^7$  K as it collapses onto large-scale structure (*e.g.*, filaments; Davé et al. 2001; Fang & Bryan 2001). The WHIM thermally emits soft X-rays; Davé et al. (2001) argue that the WHIM must be in a filamentary structure to agree with the soft X-ray background. Collisional ionization dominates in high-temperature, high-density regions (*e.g.*, WHIM), and photoionization dominates in low-temperature, low-density regions (*e.g.*, local Ly $\alpha$  forest; Fang & Bryan 2001). Cen & Ostriker (2006) and Cen & Fang (2006) include new and improved prescriptions for galactic super-winds and collisional non-equilibrium. Their recent results substantiate previous simulations which argue for a large contribution of WHIM gas to the baryonic census as well as demonstrate the importance of galactic super-winds in dispersing metals to large distances from the galaxies, with impact parameters  $\rho \approx 1$  Mpc.

Several observational papers propose that O VI absorption occurs in a multi-phase medium, with hot collisionally ionized components ( $10^5 \lesssim T \lesssim 10^7$  K) and warm photoionized components ( $T \approx 10^4$  K) (*e.g.* Tripp et al. 2000; Simcoe et al. 2002; Shull et al. 2003; Sembach et al. 2004a; Danforth et al. 2006). Other papers suggest that the O VI absorbers are in collisional ionization equilibrium (CIE; Richter et al. 2004), not in

<sup>1</sup> Department of Astronomy; University of California; 1156 High St., Santa Cruz, CA 95064; kcooksey@ucolick.org

<sup>2</sup> UCO/Lick Observatory; University of California; 1156 High St., Santa Cruz, CA 95064; xavier@ucolick.org

<sup>3</sup> Department of Astronomy; University of Chicago; 5640 S. Ellis Ave., Chicago, IL 60637; hchen@oddjob.uchicago.edu

<sup>4</sup> Observatories of the Carnegie Institution of Washington; 213 Santa Barbara St., Pasadena, CA 91101; mulchae@ociw.edu

<sup>5</sup> Steward Observatory, University of Arizona, 933 N. Cherry Ave., Tucson, AZ 85721; bjw@as.arizona.edu

equilibrium (Tripp & Savage 2000), or photoionized and therefore not part of the WHIM (Prochaska et al. 2004). Richter et al. (2004) argue that broad Ly $\alpha$  features can be used to trace the WHIM if there are no O VI lines, and the simulations of Richter et al. (2006) indeed find broad Ly $\alpha$  features at the redshift of O VI absorption.

Recent observations have argued that O VI absorbers are often correlated with galaxies or galaxy groups (*e.g.*, Richter et al. 2004; Prochaska et al. 2004; Sembach et al. 2004a). Typically, O VI absorbers are identified because Ly $\alpha$  absorbers were first identified at the corresponding redshifts. If O VI absorption were truly tracing the WHIM, the hydrogen should be predominantly ionized at  $T \approx 10^5$  K and therefore very broad and shallow due to thermal broadening, precluding easy detection (Richter et al. 2004). This may explain the tendency to detect O VI absorbers near galaxies and to model the absorbers as a multi-phase medium.

Danforth & Shull (2005) and Danforth et al. (2006, hereafter, DRS06) surveyed the *Hubble Space Telescope* Space Telescope Imaging Spectrograph (STIS) and *Far Ultraviolet Spectroscopic Explorer* (*FUSE*) archives for Ly $\alpha$ , O VI, and C III  $\lambda$ 977. Of 45 Ly $\alpha$  absorbers with statistics for both metal lines, 12 (27%) have both O VI and C III absorption, 8 (18%) have O VI without C III, and 4 (9%) have C III without O VI. The prevalence of low-ionization absorption Ly $\alpha$  and, often, C III associated with highly ionized O VI absorption supports a multi-phase model of the IGM. DRS06 did not perform a blind search for O VI without Ly $\alpha$  absorbers.

Presented here is a detailed analysis of far-ultraviolet STIS and *FUSE* spectra of the quasar PKS1302–102 ( $z_{QSO} = 0.2784 \pm 0.0005$ , Corbett et al. 1998). Column densities are measured for H I Lyman systems and metal lines. For systems with at least Ly $\alpha$  and Ly $\beta$ , the H I Doppler parameter was measured. The redshift density of Ly $\alpha$ , O VI, and C III absorbers is determined. A direct comparison with the results of DRS06 is given. In addition, the UV spectra are complemented by a galaxy survey of the field surrounding PKS1302–102, made at Las Campanas Observatory. These observations are used to characterize the O VI absorbers and other metal-line systems with respect to galaxies. This is the first in a series of papers on the chemical enrichment of the low-redshift IGM (*HST* proposal 10679; PI: J. X. Prochaska). The paper is organized as follows: the data and reduction procedures are discussed in § 2; the identification of absorption-line systems in § 3; metal-line systems in § 4; strong Ly $\alpha$  absorbers in § 5; previous analysis in § 6; galaxy survey and results in § 7; and final discussion and conclusions in § 8.

## 2. DATA AND REDUCTION

### 2.1. Space Telescope Imaging Spectrograph

PKS1302–102 was observed for a total of 22 ks by the *Hubble Space Telescope* Space Telescope Imaging Spectrograph (*HST* STIS) in August 2001 (Program 8306; PI: M. Lemoine). The observations are summarized in Table 1. STIS observations were taken with the medium echelle grating E140M, which covers  $1140 \lesssim \lambda \lesssim 1730$  Å. The 44 orders were coadded individually before being coadded into a one-dimensional spectrum, which was used for further analysis. There are gaps between the orders for  $\lambda \gtrsim 1600$  Å. STIS E140M has a resolution of  $R \approx 45,000$ ,

or FWHM  $\approx 7$  km s $^{-1}$ . More information about STIS can be found in Mobasher (2002).

The data were retrieved from the Multimission Archive of Space Telescope (MAST)<sup>6</sup> and were reduced with CalSTIS v2.18 with On-the-Fly-Reprocessing. The multiple exposures were coadded with the IDL routine COADSTIS from the XIDL library,<sup>7</sup> which is described below. Each order of each exposure was rebinned to the same logarithmic wavelength solution. Regions with bad data quality flags and a small neighboring buffer to the bad regions were excluded in the coadding of the observations. The STIS Data Handbook defines many data quality flags (Mobasher 2002), and all but three non-zero flags were rejected (16, 32, and 1024). These three accepted flags indicated abnormally high dark rate and mild CCD blemishes.

The spectra were scaled to the spectrum with the highest signal-to-noise ratio S/N, measured across all orders. The orders were coadded with the XIDL routine X\_COMBSPEC, which weights by S/N. To coadd the orders into one spectrum, overlapping regions of the orders were combined by taking the weighted mean of the flux.

### 2.2. Far Ultraviolet Spectroscopic Explorer

PKS1302–102 was observed for a total of 149 ks with the *Far Ultraviolet Spectroscopic Explorer* (*FUSE*) between May 2000 and January 2001 (Program P108; PI: K. Sembach). The raw *FUSE* files, also downloaded from MAST, were completely reduced with a modified CalFUSE<sup>8</sup> v3.0.7 pipeline and coadded with Don Lindler's IDL tool FUSE\_REGISTER.

*FUSE* covers the wavelength range  $905 \lesssim \lambda \lesssim 1190$  Å with  $R \approx 20,000$ , or FWHM  $\approx 15$  km s $^{-1}$ . The four gratings of *FUSE* disperse onto two detectors resulting in eight spectra per exposure. More details about the *FUSE* instrument and mission can be found in Moos et al. (2000) and Sahnou et al. (2000). All PKS1302–102 *FUSE* observations were taken in photon address mode (*i.e.*, time-tag mode) with the low-resolution aperture (LWRS).

The two separate observations of PKS1302–102 were coadded into one set of eight spectra in order to increase S/N. The CalFUSE pipeline has procedures for this purpose. After each exposure has been processed, the intermediate data files (IDFs), which contain all information from the raw photon-event list to the wavelength solution, are combined into one IDF; in a similar manner, the bad pixel masks (BPMs) are also combined. From these two files, the CalFUSE pipeline extracts the final, calibrated spectra.

By default, the combined IDF has its aperture centroid defined by the first, single-exposure IDF in the list to be combined. In addition, to save space, the combined BPM is only defined for the regions of the two-dimensional spectra used in the final extraction (*i.e.*, aperture and background windows). Each single *FUSE* exposure of PKS1302–102 has low S/N and a poorly measured centroid, and CalFUSE was not able to optimally extract the final spectra. Even if they were optimally-extracted, the spectra would exclude good data since the centroid

<sup>6</sup> <http://archive.stsci.edu/>

<sup>7</sup> <http://www.ucolick.org/~xavier/IDL/>

<sup>8</sup> <ftp://fuse.pha.jhu.edu/fuseftp/calfuse/>

TABLE 1  
 OBSERVATIONS SUMMARY

Instrument	Obs. Date	Data ID	$T_{\text{obs}}^{\text{a}}$ (ks)	$N_{\text{exp}}^{\text{b}}$	Aperture/Grating	S/N (per pixel)
FUSE	2000-05-21	P108020	66.0	31	LWRS	2.7 <sup>c</sup>
FUSE	2001-01-20	P108020	83.3	34	LWRS	3.7 <sup>c</sup>
STIS	2001-08-21	8306	22.1	2	0.2X0.2/E140M	3.2

<sup>a</sup> Total observation time for coadded spectrum<sup>b</sup> Total number of exposures per observation<sup>c</sup> Best signal-to-noise ratio measured for LiF 1B

used was not measured for the combined IDF.

To properly calculate the centroid for a combined IDF, several subroutines were copied from the CalFUSE program CF\_EDIT, which is an IDL GUI used to modify IDFs, into a customized IDL routine that calculates the centroid and modifies the IDF header accordingly. This new centroid was written to the headers of the individual IDFs so that the BPMs generated with the standard CalFUSE pipeline would automatically span the desired regions of the spectra. These BPMs were combined, as mentioned previously, and used with the combined IDF to extract the calibrated spectra. In this manner, the PKS1302–102 *FUSE* spectra were optimally extracted.

The calibrated spectra from each observation were coadded with FUSE\_REGISTER. The eight segments were not combined into one spectrum. This allowed for the identification of the same feature in different segments for confidence and avoids the issue that the *FUSE* channels have slightly different wavelength solutions. Values quoted in this paper primarily come from the detection in the channel with the highest S/N.

According to the *FUSE* white paper about wavelength calibration<sup>9</sup>, the two main sources of uncertainty in the absolute wavelength solution are the detector distortions and zero-point offsets, which, at worst, cause uncertainties of  $\delta v \approx 13 \text{ km s}^{-1}$  and  $\approx 66 \text{ km s}^{-1}$ , respectively. The STIS wavelength solution is accurate to  $\delta v \approx 4 \text{ km s}^{-1}$  (Mobasher 2002). The partial Lyman-limit system at  $z_{\text{abs}} = 0.09487$  spanned all the *FUSE* channels, save SiC 1B (see § 4.5), and was used to shift the *FUSE* spectra onto the STIS wavelength solution. The alignment of the Galactic features is secondary evidence that the shifts are reasonable. For SiC 1B, the Galactic Ly $\gamma$  emission was used. The spectra were shifted by the following amounts:  $-56 \text{ km s}^{-1}$  (SiC 1B);  $35 \text{ km s}^{-1}$  (SiC 2A);  $9 \text{ km s}^{-1}$  (LiF 2B);  $21 \text{ km s}^{-1}$  (LiF 1A);  $-22 \text{ km s}^{-1}$  (SiC 1A);  $18 \text{ km s}^{-1}$  (LiF 1B); and  $2 \text{ km s}^{-1}$  (LiF 2A).

The SiC 2B and LiF 2B segments were not used in the analysis due to their poor sensitivity. The other three SiC channels have poor flux zero points, resulting in negative flux and uncertain  $W_r$ ; however, line identification was possible. SiC 1A was excluded from analysis because LiF 1A covered the same wavelength range; SiC 1B and 2A were included to cover the lower wavelengths. There are two segments covering most wavelengths:  $905 \lesssim \lambda \lesssim 1005 \text{ \AA}$  (SiC 2A and 1B);  $990 \lesssim \lambda \lesssim 1090 \text{ \AA}$  (LiF 1A); and  $1088 \lesssim \lambda \lesssim 1188 \text{ \AA}$  (LiF 1B and 2A).

### 2.3. Continuum Fitting

The spectra were normalized with a parameterized b-spline continuum-fitting program. Once an initial breakpoint spacing was chosen ( $\approx 6 \text{ \AA}$  for STIS and  $\approx 4\text{--}5 \text{ \AA}$  for *FUSE*), the spectrum was iteratively fit with a b-spline. In each iteration, pixels that lay outside the high/low sigma clips (*e.g.*,  $2.5/2$ ) were masked out to prevent absorption features, cosmic rays, or other bad pixels from skewing the fit. This process was repeated until the fit changed less than a set tolerance compared to the previous iteration. The breakpoint spacing was automatically decreased in regions of great change (*e.g.*, quasar Ly $\alpha$  emission) and increased in regions of relatively little variation. More specifically, the spacing is made coarser in regions where the binned flux  $f_i$  varied by  $\leq 10\%$  compared to the error-weighted flux  $\bar{f}$ ; the spacing is refined where  $f_i$  varied by greater than one standard deviation  $\sigma_{f_i}$  of  $\bar{f}$ . The value  $f_i$  is the median flux in bins defined by the initial breakpoint spacing. The spectrum and its error were divided by the continuum to generate the normalized spectrum used in the analysis.

The program may loosely be considered “automatic:” it will converge on the best fit for the spectrum based on a given set of parameters. However, a fit based on a random set of parameters may not be a good fit to the continuum as judged visually by the authors. To estimate the errors resulting from the subjective nature of continuum fitting, we fit the spectra “by-hand” with the XIDL routine X\_CONTINUUM and compared the change in rest equivalent width  $W_r$  values. The  $W_r$  values measured from the spectra normalized by the automated program are in good agreement with those measured from the spectra normalized by hand. The root-mean-squared (RMS) fractional difference is  $< 5\%$  for STIS and  $12\%$  for *FUSE*. For column densities, the RMS fractional difference is  $< 1\%$  for both instruments.

## 3. ABSORPTION-LINE SYSTEMS

### 3.1. Identifying Systems

We search for IGM absorption systems—absorption lines physically associated with one another—with allowance for variations in *e.g.*, ionizing mechanism, density, temperature. The absorption features detected in the *FUSE* and STIS spectra were sorted into Galactic lines and intergalactic absorption lines. The latter category was further sorted into their respective systems by comparing their redshifts, line profiles, and rest equivalent width  $W_r$  ratios. Lines of the same ionized species from a given absorption system should have the same redshift, similar line profiles, and unsaturated  $W_r$  values that scale with oscillator strengths (see Figures 1 and 2). Ions from the same phase of the IGM tend to have roughly the same redshift and similar profiles. For example, H I and C III of  $z_{\text{abs}} = 0.04226$  are well aligned

<sup>9</sup> [http://fuse.pha.jhu.edu/analysis/calfuse\\_wp1.html](http://fuse.pha.jhu.edu/analysis/calfuse_wp1.html)

in velocity space, and have similar asymmetric profiles, whereas O VI is at a different redshift (velocity) and has a dissimilar profile (see Figure 3); this suggests the H I and C III absorption arises from one phase of the IGM and O VI from another.

In order to thoroughly identify the absorption features in the spectra of PKS1302–102, we developed an automated procedure to detect all features in the spectra greater than a minimum significance and width. We then interactively identified the features not coincident with Galactic lines.

### 3.1.1. Automatic Line Detection and Doublet Search

A purely interactive search (as described below) would be biased towards systems with Ly $\alpha$ . O VI ions that are associated with collisionally ionized gas at  $T \approx 3 \times 10^5$  K (*e.g.*, the canonical WHIM) are likely to have associated Ly $\alpha$  profiles that are broad and shallow (Richter et al. 2004). The PKS1302–102 spectra does not have sufficient S/N to reliably detect broad Ly $\alpha$  features. To avoid biasing the search against warm-hot O VI gas, we searched for doublets independently of Ly $\alpha$ .

In order to conduct a blind search for pairs, primarily doublets like O VI, an automated feature-finding program was developed to detect all possible absorption features with a minimum significance  $\sigma_{min}$  and width. The spectrum was first convolved with a Gaussian with FWHM  $b_{min}$ . The convolved pixels were grouped into potential features with significance  $\sigma_{pix} \geq \sigma_{min}$ . The final result is a list of central wavelengths, observed equivalent width  $W_{obs}$  and error, and wavelength limits (used to measure  $W_{obs}$ ).

Next, a blind search for doublets (O VI, C IV, N V, and Si IV) was performed. The search assumed each automatically detected feature between Galactic and quasar O VI could be O VI 1031 and only identified a possible pair when another feature was at the appropriate wavelength spacing within the bounds of  $\lambda 1031$  translated to the appropriate, redshifted wavelength of  $\lambda 1037$ . This procedure was repeated for the C IV, N V, and Si IV doublets and for Ly $\alpha$ , Ly $\beta$  and Ly $\alpha$ , C III pairs.

The blind doublet search successfully identified Galactic O VI, C IV, N V, and Si IV as well as the IGM O VI systems at  $z_{abs} = 0.04226$ ,  $0.06468$ , and  $0.09487$ , verified by the interactive search. The search also resulted in a possible O VI doublet at  $z_{abs} = 0.01583$  with Ly $\alpha$  not detected at  $3\sigma$ . However, this candidate O VI doublet is actually the coincidence of Galactic Ar I 1048 and H $_2$  1054.0 R(3). In this case, the misidentification was evident from the fact that the  $W_r$  ratio was inconsistent with an O VI doublet.

### 3.1.2. Interactive Search

The automatic line-detection procedure described above generates a list of unidentified features meeting a specified minimum requirement. The features may be Galactic, intergalactic, or, in a few cases, spurious. The automated pair searches (*e.g.*, Ly $\alpha$ , Ly $\beta$ ) supply a starting point for interactively identifying the features and sorting them into IGM absorption systems.

Identifying the absorption lines first required disentangling Galactic from intergalactic features. The velocity plots of the Ly $\alpha$ , Ly $\beta$  pairs from the blind search were examined individually. If these pairs were well aligned

in velocity space, with similar line profiles, and decreasing  $W_r$ , we interactively searched for higher-order Lyman lines (*e.g.*, Ly $\gamma$ , Ly $\delta$ ) and/or common metal lines, redshifted by the assumed-Ly $\alpha$  redshift. These lines were grouped as a possible system. The rough priority of metal lines was: (a) C III, O VI, C IV  $\lambda\lambda 1548, 1550$ ; (b) N II  $\lambda 1083$ , Si III  $\lambda 1206$ , C II  $\lambda 1036$  or  $\lambda 1334$ ; and (c) N III  $\lambda 989$ , Si IV  $\lambda\lambda 1393, 1402$  (using atomic data listed in Prochaska et al. 2004). In this initial search, no knowledge of the Galactic lines biased the identification of IGM absorption lines.

Second, all features from the automatic search corresponding to likely Galactic lines were recorded as such, regardless (for now) whether the same features were first identified as IGM lines. The likely Galactic lines included various ionization states of iron, oxygen, nitrogen, sulfur, carbon, silicon, phosphorus, argon, and aluminum. This set of lines was defined in a stacked spectrum of normalized STIS E140M spectra of 15 low-redshift quasars. In the *FUSE* channels with  $\lambda \lesssim 1000$  Å, molecular hydrogen lines are abundant due to the Lyman and Werner bands. The PKS1302–102 sight line has moderate to low molecular hydrogen absorption with a line of sight  $\log N(\text{H}_2) = 16.3$  (Wakker 2006).

All automatically detected features not already identified as Galactic or associated with an intergalactic system was assumed to be Ly $\alpha$  if between Galactic Ly $\alpha$  and Ly $\alpha$  at the redshift of PKS1302–102 (*i.e.*,  $1216 \lesssim \lambda \lesssim 1563$  Å). For example, the strong Ly $\alpha$  absorber at  $z_{abs} = 0.19242$  was detected automatically, not paired with another feature, and not corresponding to a Galactic line.

For spectra of low-redshift quasars, line confusion (*e.g.*, blends) is minimal. However, line coincidences do occur. As an example, consider the Lyman series at  $z_{abs} = 0.09400$ , which first appeared to be an especially strong H I absorber. The Ly $\beta$ , Ly $\gamma$ , and Ly $\delta$  transitions were blended with Galactic lines, and higher-order Lyman lines were confused with H $_2$  absorption and with the higher-order Lyman lines at  $z_{abs} = 0.09487$ . Occasional blends also occur between different IGM absorption systems. We disentangle these blends assuming common line-strengths for the various transitions within a blend, allowing for modest variations. For instance, DRS06 lists a Ly $\alpha$  absorber at  $z_{abs} = 0.08655$ , whereas we identify it as Si III at  $z_{abs} = 0.09487$  because the would-be Ly $\beta$  at  $z_{abs} = 0.08655$  was less than  $3\sigma$  significance and the system at  $z_{abs} = 0.09487$  is a strong H I absorber expected to have associated metal-line absorption.

Throughout this paper, only the statistical errors from photon counting are quoted, but the true errors should account for the combined statistical, continuum, and systematic errors. An estimate of the combined error will change the detection limit with respect to the statistical error. In § 2.3, we estimated the RMS fractional difference due to continuum fitting to be  $< 5\%$  for STIS and  $12\%$  for *FUSE*. The rest equivalent width is measured with a simple boxcar summation. The wavelength limits of the boxcar window were defined interactively and are subjective. The RMS fractional difference due to changing the window by  $15\%$  is  $6\%$  for STIS and  $13\%$  for *FUSE*. Column densities were affected by less than  $1\%$  by changing the window.

TABLE 2  
 $W_r$  SUMMARY

Ion	$\lambda_{obs}$ (Å)	$\lambda_r$ (Å)	$z_{abs}$	$W_1$ (mÅ)	$\sigma(W_1)$ (mÅ)	$W_2$ (mÅ)	$\sigma(W_2)$ (mÅ)	$W_f$ (mÅ)	$\sigma(W_f)$ (mÅ)
<i>FUSE</i>									
H I 930	934.798	930.748	0.00435	168	47	74	37	110	29
H I 937	941.898	937.803	0.00437	293	60	247	40	262	33
H I 949	953.995	949.743	0.00448	418	68	305	38	332	33
H I 972	976.903	972.537	0.00449	367	86	350	44	353	39
H I 937	977.333	937.803	0.04215	7	74	15	44	13	38
C III 977	981.309	977.020	0.00439	7	63	156	41	111	35
H I 949	989.770	949.743	0.04214	349	81	584	37	542	34

NOTE. — Note that the list is incomplete for wavelengths  $< 1000\text{Å}$  where the data has poor S/N and significant line blending. Columns 4,5 (6,7) refer to the SiC 1B (SiC 2A) channel for  $905 < \lambda < 1005\text{Å}$ ; LiF1A for  $990 < \lambda < 1090\text{Å}$ ; LiF 1B (LiF 2A) for  $1088 < \lambda < 1188\text{Å}$ ; and STIS E140M for  $\lambda > 1188\text{Å}$ . [The complete version of this table is in the electronic edition of the Journal. The printed edition contains only a sample.]

The errors from the continuum fitting and boxcar summation are correlated, but as a first approximation, we will add them in quadrature. Ultimately, for a feature to be detected at three times the combined error, the feature must be detected at  $3.1\sigma$  for STIS and  $3.6\sigma$  for *FUSE*, where  $\sigma$  is the statistical error only. For example, C III at  $z_{abs} = 0.00442$  is a  $3.2\sigma$  detection, but folding in the 12% continuum-fitting and 13% boxcar-summation errors for *FUSE*, the feature is 2.8 times the combined error. Ly $\alpha$  at  $z_{abs} = 0.04621$  is a similar case in the STIS spectrum. The majority of lines discussed in this paper have significance greater than three times the combined error, and we will use  $3\sigma$ , commonly quoted in the literature, as our detection limit knowing a more rigorous examination of our errors does not affect our results.

There are 23 Ly $\alpha$  features detected at  $\geq 3\sigma$  significance in the spectra of PKS1302–102. Of these, 14 are strong Ly $\alpha$  absorbers with  $\log N_{\text{HI}} \geq 14$  (61%) and seven with at least one metal line (30%). There are three probable O VI systems. Line identification is complete to 95% in the region of STIS where intergalactic Ly $\alpha$  could be detected with  $\sigma_{min} = 4\sigma$  and  $b_{min} = 20\text{ km s}^{-1}$ ,<sup>10</sup> and identification is complete to  $> 80\%$  in *FUSE* LiF 2A, 1B, and 1A for  $b_{min} = 40\text{ km s}^{-1}$  features. Completeness was measured by correlating the identified lines from the interactive search with the automatically detected features discussed above.

### 3.2. Column Densities, Doppler Parameters, and Metallicities

For absorption systems exhibiting at least two members of the H I Lyman series, the H I column density  $\log N_{\text{HI}}$  and Doppler parameter  $b$  were measured with a curve-of-growth (COG) analysis of the  $W_r$  values that minimized  $\chi^2$ . For metal lines, the apparent optical depth method (AODM) was used to measure the column densities (Savage & Sembach 1991).

To measure metallicities, we used ionization corrections from collisional ionization equilibrium (CIE) or photoionization models of the metal-line systems, cal-

culated with CLOUDY<sup>11</sup> versions 94 and 06.02.09a, respectively, as last described by Ferland et al. (1998). The CIE models are described in Prochaska et al. (2004).

To construct the photoionization models, the medium was assumed to be a plane-parallel slab ionized by a Haardt & Madau (1996, updated in 2005) quasar-only ultraviolet background. The number density of hydrogen  $n_{\text{H}}$  was assumed to be  $0.1\text{ cm}^{-3}$ , though our models are insensitive to this parameter since we are in the optically-thin regime. The ionization parameter  $\log U$ , metallicity  $[\text{M}/\text{H}]$ ,<sup>12</sup> neutral column density  $\log N_{\text{HI}}$ , and redshift of the UV background were varied to sample the parameter space. The ionization parameter is a dimensionless ratio of the number of hydrogen-ionizing photons to the total number of hydrogen atoms.

Abundance-independent ionic ratios of the same metal (*e.g.*,  $\text{N}(\text{C}^{++})/\text{N}(\text{C}^{+3})$ ) and/or abundance-dependent ratios of metals with similar ionization potentials (*e.g.*,  $\text{N}(\text{C}^{+3})/\text{N}(\text{O}^{+5})$ ) constrained  $\log U$  or  $T$  (see § 4.5). The  $\log U$  or  $T$  limits define the ionization corrections for the measured metallicities (*e.g.*,  $[\text{C}/\text{H}]$ ). Due to the simplifications and assumptions in the CLOUDY models, the model abundances and metallicities are reliable to within a factor of two.

Modeling of a multi-phase medium was generally not considered because the systems presented in this paper simply have too few metal lines. By the same token, multi-phase and collisional ionization *non-equilibrium* scenarios are not ruled out by the observations. In select cases where the kinematics and abundances suggest a multi-phase medium, we do use photoionization and CIE models to describe the different components.

## 4. METAL-LINE SYSTEMS

This section summarizes the seven Ly $\alpha$  systems with at least one metal line detected. Velocity plots, COG analysis, and CLOUDY models for each system are discussed. Four of the seven systems have C III absorption only, one with C III and the O VI doublet, one with tentative C III and O VI detections, and one with C III, Si III, and a broad O VI doublet. Because C III is the

<sup>10</sup> The remaining 5% of the automatically identified features that could be Ly $\alpha$  appear to be spurious.

<sup>11</sup> <http://www.nublado.org>

<sup>12</sup>  $[\text{M}/\text{H}] = \log(\text{N}(\text{M})/\text{N}(\text{H})) - \log(\text{N}(\text{M})/\text{N}(\text{H}))_{\odot}$

TABLE 3  
IONIC COLUMN DENSITIES

Ion	$\lambda_r$ (Å)	$W_r$ (mÅ)	$\log N_{AODM}$	$\log N_{adopt}$
$z_{abs} = 0.00442, \log N_{HI} = 15.77 \pm 0.35$				
C II	1334.5323	< 64	< 13.71	< 13.71
C III	977.0200	$111 \pm 35$	> 13.48	> 13.48
C IV	1548.1950	< 81	< 13.44	< 13.44
C IV	1550.7700	< 59	< 13.70	...
$z_{abs} = 0.04226, \log N_{HI} = 15.07 \pm 0.08$				
C II	1334.5323	< 58	< 13.70	< 13.70
C III	977.0200	$168 \pm 12$	$13.66 \pm 0.05$	$13.66 \pm 0.05$
C IV	1548.1950	< 173	< 14.38	< 13.84
C IV	1550.7700	< 80	< 13.84	...
O I	1302.1685	< 56	< 14.15	< 14.15
O VI	1031.9261	$190 \pm 18$	$14.42 \pm 0.05$	$14.47 \pm 0.04$
O VI	1037.6167	$173 \pm 15$	$14.65 \pm 0.06$	...
$z_{abs} = 0.06468, \log N_{HI} = 14.47 \pm 0.10$				
C III	977.0200	< 56	< 13.09	< 13.09
C IV	1548.1950	< 107	< 13.76	< 13.76
C IV	1550.7700	< 111	< 14.09	...
O I	1302.1685	< 55	< 14.07	< 14.07
O VI	1031.9261	$47 \pm 11$	$13.75 \pm 0.08$	$13.81 \pm 0.06$
O VI	1037.6167	$42 \pm 10$	$13.96 \pm 0.09$	...
$z_{abs} = 0.09400, \log N_{HI} = 15.05 \pm 0.06$				
C II	1334.5323	< 60	< 13.64	< 13.64
C III	977.0200	$80 \pm 9$	> 13.26	> 13.26
C IV	1548.1950	< 106	< 14.01	< 14.01
C IV	1550.7700	< 101	< 14.78	...
$z_{abs} = 0.09487, \log N_{HI} = 16.87 \pm 0.03$				
C II	1334.5323	< 80	< 13.90	< 13.90
C III	977.0200	$243 \pm 13$	> 13.89	> 13.89
C IV	1548.1950	< 130	< 14.11	< 14.11
C IV	1550.7700	< 135	< 15.44	...
O I	1302.1685	< 76	< 14.23	< 14.23
O VI	1031.9261	$97 \pm 14$	$14.00 \pm 0.06$	$14.03 \pm 0.05$
O VI	1037.6167	$42 \pm 13$	$14.12 \pm 0.08$	...
Si II	1260.4221	< 45	< 12.78	< 12.78
Si III	1206.5000	$172 \pm 16$	$13.11 \pm 0.07$	$13.11 \pm 0.07$
Si IV	1393.7550	< 53	< 13.00	< 13.00
Si IV	1402.7700	< 58	< 13.29	...
$z_{abs} = 0.14529, \log N_{HI} = 15.29 \pm 0.02$				
C II	1036.3367	< 38	< 13.75	< 13.74
C II	1334.5323	< 59	< 13.74	...
C III	977.0200	$66 \pm 10$	$13.15 \pm 0.06$	$13.15 \pm 0.06$
O I	1302.1685	< 65	< 14.21	< 14.21
O VI	1031.9261	< 115	< 14.18	< 14.18
$z_{abs} = 0.19156, \log N_{HI} = 15.27 \pm 0.03$				
C II	1036.3367	< 54	< 13.98	< 13.64
C II	1334.5323	< 55	< 13.64	...
C III	977.0200	$47 \pm 10$	$13.07 \pm 0.08$	$13.07 \pm 0.08$
O I	1302.1685	< 47	< 14.01	< 14.01
O VI	1031.9261	< 73	< 14.06	< 14.06
O VI	1037.6167	< 57	< 14.24	...

dominant line in photoionized gas, it may be more readily detected in the moderate S/N PKS1302–102 spectra. The metal-line systems are summarized in Table 3.

All but one of the metal-line systems have  $\log N_{HI} \geq 15$ . The two systems with multiple metal lines are likely multi-phase based on kinematic arguments (*e.g.*, velocity offsets, line profiles) and the poor fit of single-phase models to the data. More specifically, a single-

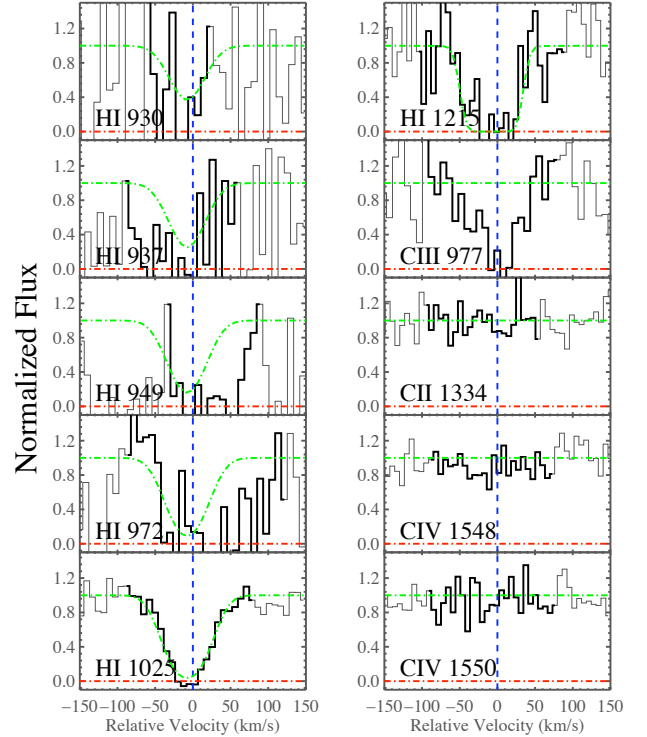


FIG. 1.— Velocity plot for  $z_{abs} = 0.00442$ . Spectra, averaged over two pixels (thin black line), are stacked in velocity space with  $v = 0 \text{ km s}^{-1}$  at  $z_{abs} = 0.00442$ , the optical-depth weighted centroid of Ly $\alpha$  (vertical blue dash line). The region used to measure  $W_r$  is highlighted (thick black line). Also indicated is the flux at zero (red dash-dot line). The H I Voigt profiles, based on the COG  $\log N_{HI}$  and  $b$  are superimposed to show the predicted area under the curve (green dash-dot line; for the metal lines, this line indicates the flux at unity). The Voigt profile centroid is fixed at the redshift of Ly $\beta$   $z_\beta = 0.00439$ . Ly $\alpha$  is detected in the wings of the damped Galactic Ly $\alpha$  feature, and the lines higher than Ly $\beta$  are detected in the SiC 2A and 1B channels, which have poor sensitivity. C II and C IV 1550 are not detected at  $3\sigma$ . Ly $\gamma$ , Ly $\delta$ , and Ly $\epsilon$  are blended with Galactic C III, H $_2$  954.0 R(4), and H $_2$  941.6 P(2).

phase, collisionally-ionized absorber does not have significant C III and O VI absorption without significant C IV absorption.

The metallicities quoted are based on ionization corrections from the best  $\log U$  or  $T$  value from the CLOUDY models with  $[M/H]$  consistent with the final, derived metallicity. In cases where the  $\log U$  value is not well constrained by the observations, we adopt a central value based on  $\log N_{HI}$ , as predicted by the empirical/theoretical relation in Prochaska et al. (2004). The nature of the galaxy environment of these systems will be discussed in § 7.

#### 4.1. $z_{abs} = 0.00442$ : C III

This metal-line system was detected at  $v = 1300 \text{ km s}^{-1}$ , in the wings of the damped Galactic Ly $\alpha$  profile (see Figure 1). The PKS1302–102 sight-line also passes through the Virgo cluster at this redshift (Wakker et al. 2003). Ly $\alpha$  and C III are well aligned in velocity space with similar line profiles, which imply the two absorbers are kinematically similar. Ly $\alpha$ , Ly $\beta$ , and Ly $\zeta$  were used to fit the COG:  $\log N_{HI} = 15.8^{+0.4}_{-0.2}$  and  $b = 17^{+2}_{-2} \text{ km s}^{-1}$  (see Figure 2).

The H I column density is not well constrained for this system. Ly $\beta$ , which was detected in LiF 1A, has the highest detection significance of the Lyman series. The

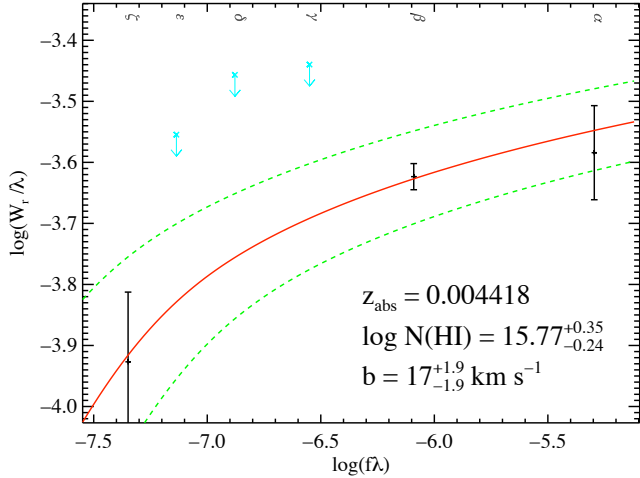


FIG. 2.— H I COG for  $z_{\text{abs}} = 0.00442$ . The best-fit curve of growth (solid red line) with  $1\sigma$  bounds (dashed green lines) is displayed over the measured  $W_r$  values included in the fit (black hashes with  $1\sigma$  error bars). Blended lines are shown as upper limits (cyan cross-top arrows). For description of the upper limits, see Figure 1. The H I Lyman lines are labeled by letter or wavelength across the top.

higher-order lines fall in the SiC 2A and 1B channels, which have poor sensitivity. The AODM HI column density for the saturated Ly $\beta$  line sets a lower limit of  $\log N_{\text{HI}} > 14.99$ . DRS06 measured  $\log N_{\text{HI}} = 14.872 \pm 0.286$  and  $b = 18 \pm 2 \text{ km s}^{-1}$  from a Voigt profile fit to Ly $\alpha$ . We examined the velocity plot with Voigt profile outlines for  $[\log N_{\text{HI}}, b] = [15.8, 17.4]$  and  $[14.87, 18]$ . The DRS06 values clearly underestimate the Ly $\beta$  absorption.

The ionic ratios  $N(\text{C}^+)/N(\text{C}^{++})$  and  $N(\text{C}^{++})/N(\text{C}^{+3})$  constrained the ionization parameter to  $-3.7 \leq \log U \leq -1.7$  for the CLOUDY models with  $\log N_{\text{HI}} = 15.75$ . For  $\log U = -2.1$ ,  $-1.9 \leq [\text{C}/\text{H}] \leq -1.6$ . From the kinematics of Ly $\alpha$  and C III and CLOUDY modeling, the  $z_{\text{abs}} = 0.00442$  system is well described as a photoionized, metal-poor, single-phase medium.

#### 4.2. $z_{\text{abs}} = 0.04226$ : O VI, C III

The Ly $\alpha$  profile shows two strong components. The blueward component aligns well with C III and the redward with O VI (see Figure 3). The H I COG for this absorber included Ly $\alpha$ , Ly $\beta$ , and Ly $\gamma$ , and the values are well constrained:  $\log N_{\text{HI}} = 15.07^{+0.08}_{-0.07}$  and  $b = 22^{+2}_{-2} \text{ km s}^{-1}$  (see Figure 4). Ly $\epsilon$ , O I  $\lambda 1302$ , C II, and C IV 1550 were not detected at  $3\sigma$ . Ly $\delta$  is blended with Galactic N III, Ly $\gamma$  with H<sub>2</sub> 1013.4 R(1), and Ly $\beta$  with C III at  $z_{\text{abs}} = 0.09400$ . O VI 1037 is blended with the weak H<sub>2</sub> 1081.7 R(3) line.

Ly $\alpha$  and C III have similar line profiles and appear well aligned in velocity space, while O VI is shifted redward. Since Ly $\alpha$  is saturated and multicomponent, its velocity is not well constrained. Taking Ly $\gamma$  as the reference line for the stronger H I component, O VI 1031 has  $\delta v_{\text{abs}} \equiv c(z_{\text{abs}} - z_{\gamma})/(1 + z_{\gamma}) = +54 \text{ km s}^{-1}$ , while C III is perfectly aligned. The significant velocity offset between the metal-line profiles suggests the metals reside in different phases of gas, with overlapping Ly $\alpha$  absorption. The O VI absorption appears associated with more tenuous H I absorption.

The  $W_r$  ratio of O VI 1031 to 1037 ( $1.1 \pm 0.13$ ) does

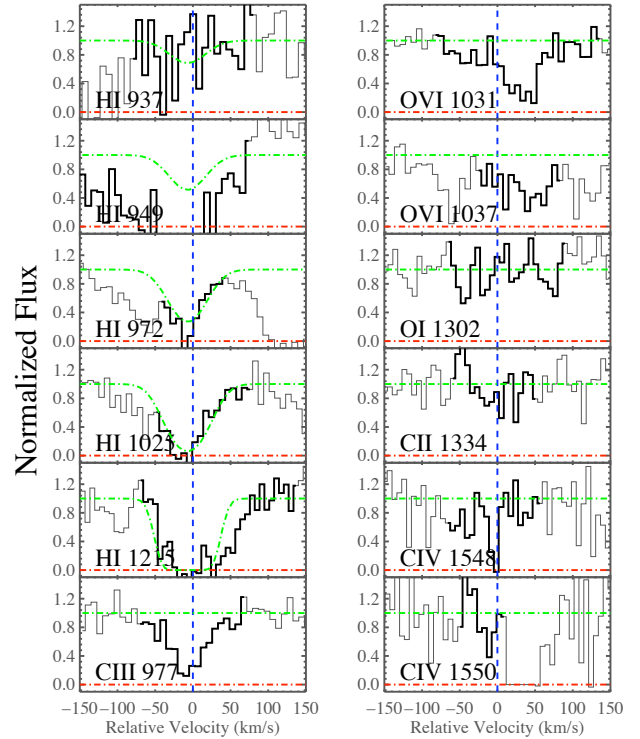


FIG. 3.— Velocity plot for  $z_{\text{abs}} = 0.04226$  (see Figure 1 description). The Ly $\alpha$  profile shows two components on either side of  $v = 0 \text{ km s}^{-1}$ . C III is more aligned with the stronger, blueward component of Ly $\alpha$ , while O VI is more aligned with the weaker, redward component. The Voigt profiles are based on a single-component COG model (see Figure 4) with centroid fixed at  $z_{\gamma} = 0.04224$ . O VI 1037 is blended with H<sub>2</sub> 1081.7 R(3) and is flanked by H<sub>2</sub> 1081.2 P(2) to the blue and Galactic F II 1081 to the red. Ly $\beta$ , Ly $\gamma$ , and Ly $\delta$  are blended (see § 4.2). Ly $\epsilon$ , O I, C II, and C IV 1550 are not detected at  $3\sigma$ . The location of C IV 1550 spans an echelle order gap in STIS.

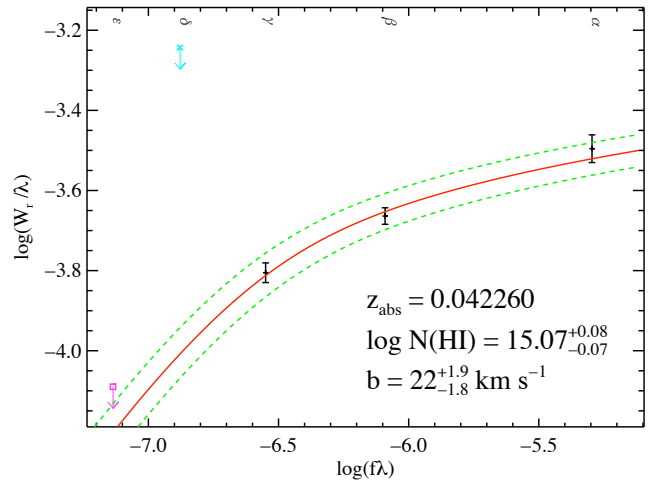


FIG. 4.— H I COG for  $z_{\text{abs}} = 0.04226$  (see Figure 2 description). Ly $\epsilon$ , which is not detected at  $3\sigma$ , is shown as a  $2\sigma$  upper limit (magenta square-top arrow). Ly $\delta$  is blended with Galactic N III.

not agree with the expected 2 : 1 ratio. The continuum fit around O VI 1037 is poorly constrained because it is at the edge of LiF 1A and there are two absorption features close to 1037. This potentially increases  $W_r$  and  $\log N(\text{O}^{+5})$ . O VI 1037 is also blended with a weak H<sub>2</sub> line. This system has the strongest O VI absorption in the PKS1302–102 sight line  $\log N(\text{O}^{+5}) = 14.5$  and

TABLE 4  
ELEMENTAL  
ABUNDANCES FOR  
ABSORBER AT  
 $z=0.04226$

Ion	[X/H]	[X/C <sup>++</sup> ]
C <sup>+</sup>	< 0.73	< 1.62
C <sup>++</sup>	-0.89	0.00
C <sup>+3</sup>	< -0.90	< -0.01
O <sup>0</sup>	< 5.60	< 6.50
O <sup>+5</sup>	-0.69	0.21

strong C III absorption  $\log N(\text{C}^{++}) = 13.7$ .

In the CLOUDY models with  $\log N_{\text{HI}} = 15$ , the ionic ratios  $N(\text{C}^+)/N(\text{C}^{++})$  and  $N(\text{C}^{++})/N(\text{C}^{+3})$  constrain  $\log U$ :  $-3.5 \leq \log U \leq -1.4$ . At the central value of  $\log U = -2.4$ , one would require  $[\text{O}/\text{C}] \approx +3$  and a super-solar O abundance to explain the column densities of C<sup>++</sup> and O<sup>+5</sup>. Therefore, we consider a single-phase model to be ruled out for low  $\log U$  values. However, a single-phase photoionization model with  $\log U = -1.5$  does give reasonable metallicities for carbon and oxygen:  $[\text{C}/\text{H}] = -0.9$  and  $[\text{O}/\text{H}] = -0.7$  (see Table 4). Also, according to Prochaska et al. (2004),  $\log U = -1.5$  is the expected value for a photoionized system with  $\log N_{\text{HI}} = 15$ . As noted above, however, the C III and O VI profiles are offset which severely challenges a single-phase model.

We have considered collisional ionization models. Under the assumption of CIE, the carbon absorption is constrained to be in a warm phase  $4.4 \times 10^4 < T < 1.1 \times 10^5$  K. Considering the limit set by  $N(\text{C}^{+3})/N(\text{O}^{+5})$ , the oxygen would be from a warm-hot phase  $T > 2.3 \times 10^5$  K with low metallicity  $[\text{O}/\text{H}] > -1.8$ . For this value, we have assumed the H I column density in the warm-hot phase is the same as measured in the COG analysis for the warm phase.

In summation, we favor a two-phase model for this systems, as strongly supported by the kinematics. C III and H I trace a photoionized phase, and O VI may trace either a photoionized or a collisionally-ionized medium.

#### 4.3. $z_{\text{abs}} = 0.06468$ : O VI

Though a tentative detection, O VI is well aligned with Ly $\alpha$  (see Figure 5). The  $W_r$  ratio of O VI 1031 to 1037 is  $1.1 \pm 0.3$ , and  $\log N(\text{O}^{+5}) = 13.8$  (see Table 3). At the redshift of Ly $\alpha$ , there is no C III detected. However, there are two features in the vicinity:  $z_{\text{abs}} = 0.09487$  Ly $\delta$  at  $\delta v_{\text{abs}} > 100 \text{ km s}^{-1}$  and H<sub>2</sub> 1040.4 P(2) at  $\delta v_{\text{abs}} \approx 0 \text{ km s}^{-1}$ , with respect to the centroid of the unsaturated Ly $\beta$ . The H<sub>2</sub> P(2) profile may be blended, and we treat the whole feature as an upper limit for C III at  $z_{\text{abs}} = 0.06468$ :  $\log N(\text{C}^{++}) < 13.1$ . O I and the C IV doublet are not detected at  $3\sigma$ .

The  $z_{\text{abs}} = 0.06468$  system has the lowest  $\log N_{\text{HI}}$  of the metal-line systems. The H I COG includes only Ly $\alpha$  and Ly $\beta$ , but the column density is well constrained because Ly $\beta$  is unsaturated:  $\log N_{\text{HI}} = 14.47_{-0.09}^{+0.1}$  and  $b = 26_{-3}^{+4} \text{ km s}^{-1}$  (see Figure 6). The upper limit to the equivalent width of Ly $\gamma$  is consistent within  $1\sigma$  of the value predicted by the COG. The H I absorption features are asymmetric and should probably be fit by a two-component COG, but the total  $N_{\text{HI}}$  value is well con-

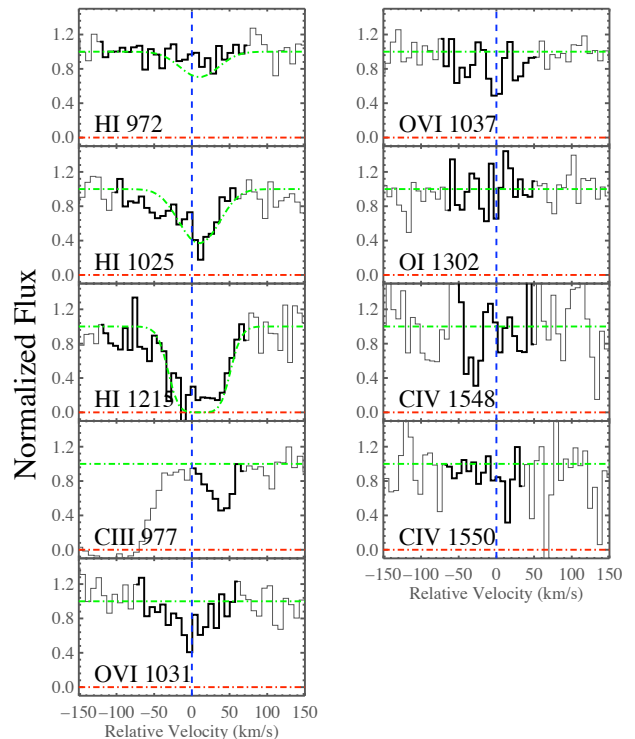


FIG. 5.— Velocity plot for  $z_{\text{abs}} = 0.06468$  (see Figure 1 description). Ly $\alpha$  has a distinct asymmetric profile, probably due to unresolved components. The O VI doublet is detected at  $\approx 4.5\sigma$ . The  $W_r$  ratio of O VI 1031 to 1037 is  $1.1 \pm 0.3$ . O I and C IV are not detected at  $3\sigma$ . C III is treated as an upper limit since it is coincident with H<sub>2</sub> 1040.4 P(2). The Voigt profile centroid is fixed at  $z_{\beta} = 0.06472$ .

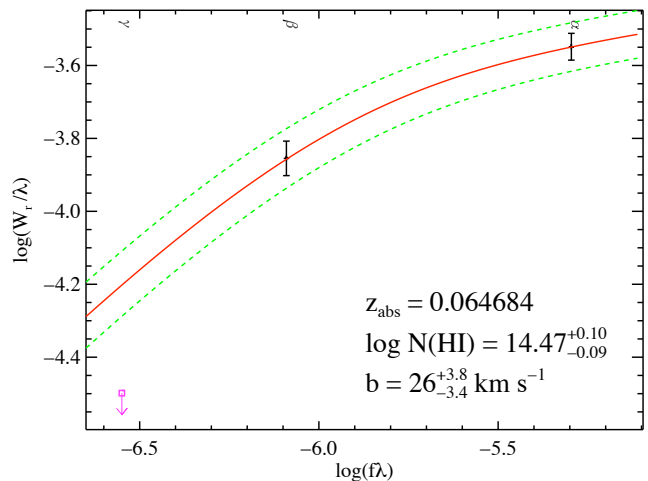


FIG. 6.— H I COG for  $z_{\text{abs}} = 0.06468$  (see Figure 2 description). Ly $\gamma$  is not detected at  $3\sigma$  but is consistent with the single-component COG fit. This H I system is possibly multi-component, as evidenced by the asymmetric Ly $\alpha$  and Ly $\beta$  profiles in Figure 5.

strained by our COG analysis.

Assuming a photoionized gas, the ionic ratio  $N(\text{C}^{++})/N(\text{O}^{+5})$  constrain  $\log U > [\text{C}/\text{O}] - 1.5$  in the CLOUDY models with  $\log N_{\text{HI}} = 14.5$ . For  $\log U = -1.2$  and assuming  $[\text{C}/\text{O}] = 0$ ,  $[\text{O}/\text{H}] > -1.2$  and  $[\text{C}/\text{H}] < -0.5$  (see Table 5). The  $z_{\text{abs}} = 0.06468$  could be a single-phase photoionized medium

A single-phase CIE model is *not* ruled out by the ob-

TABLE 5  
ELEMENTAL  
ABUNDANCES FOR  
ABSORBER AT  
 $z=0.06468$

Ion	[X/H]	[X/O <sup>+5</sup> ]
C <sup>++</sup>	< -0.52	< 0.63
C <sup>+3</sup>	< -0.29	< 0.87
O <sup>0</sup>	< 6.44	< 7.59
O <sup>+5</sup>	-1.15	0.00

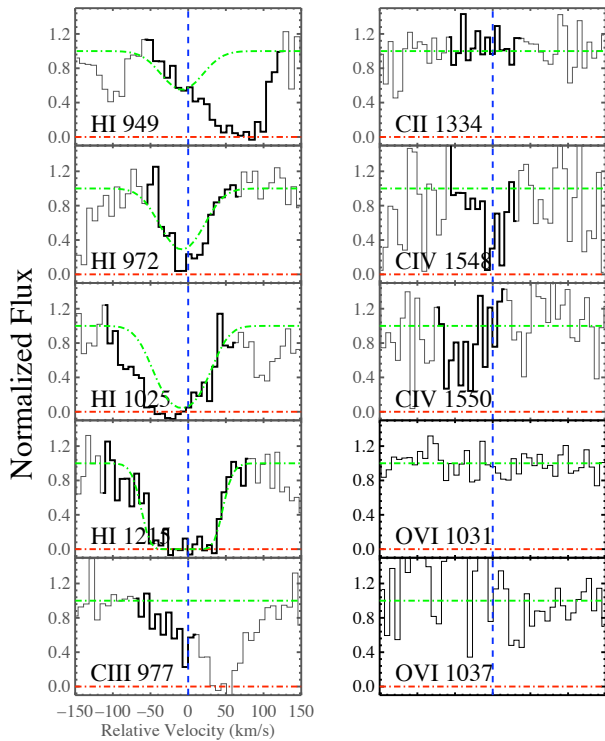


FIG. 7.— Velocity plot for  $z_{abs} = 0.09400$  (see Figure 1 description).  $\text{Ly}\beta$ ,  $\text{Ly}\gamma$ , and  $\text{Ly}\delta$  are blended with Galactic Fe II 1121, Galactic Fe II 1064, and Galactic O I 1039, respectively. C III is blended with  $\text{Ly}\beta$  at  $z_{abs} = 0.04226$ . C II and the C IV doublet are not detected at  $3\sigma$ . The region where the O VI doublet would be is shown. The Voigt profile centroid is fixed at  $z_\gamma = 0.09397$ .

servations.  $N(\text{C}^{+3})/N(\text{O}^{+5})$  constrains  $T \geq 1.9 \times 10^5$  K, for which  $[\text{O}/\text{H}]$  and  $[\text{C}/\text{H}]$  would be the same as above. This system may represent a detection of the WHIM because of its temperature and the non-detection of C IV absorption.

#### 4.4. $z_{abs} = 0.09400$ : C III

$\text{Ly}\beta$  and  $\text{Ly}\delta$  are significantly blended with Galactic Fe II 1121 and Galactic O I 1039, respectively (see Figure 7).  $\text{Ly}\gamma$  is somewhat blended with Galactic Fe II 1064. The degree of blending is apparent from the line profiles in Figure 7 as well as a velocity plot of the Galactic lines (not shown). The COG includes only  $\text{Ly}\alpha$  and the blended  $\text{Ly}\gamma$  and yields an upper limit:  $\log N_{\text{HI}} \leq 15.05$  for  $b = 28^{+2}_{-2}$  km s<sup>-1</sup> (see Figure 8).

C III is blended with  $\text{Ly}\beta$  at  $z_{abs} = 0.04226$ , though the part included in Figure 7 is well aligned. Since C III is partially deblended, there is a lower limit on the column density  $\log N(\text{C}^{++}) > 13.3$  from the AODM (see Table 3). C II and the C IV doublet are not detected at  $3\sigma$ .

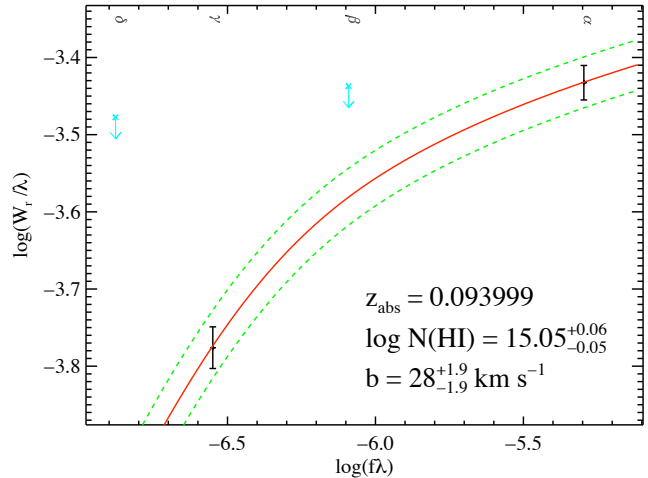


FIG. 8.— H I COG for  $z_{abs} = 0.09400$  (see Figure 2 description). The COG analysis only includes  $\text{Ly}\alpha$  and  $\text{Ly}\gamma$  because  $\text{Ly}\beta$  and  $\text{Ly}\delta$  were blended (see Figure 7).  $\text{Ly}\gamma$  is blended with a weak Galactic line. Therefore, we conservatively consider the best fit to be an upper limit.

In the CLOUDY models with  $\log N_{\text{HI}} = 15$ , the ionic ratios  $N(\text{C}^+)/N(\text{C}^{++})$  and  $N(\text{C}^{++})/N(\text{C}^{+3})$  constrain the ionization parameter:  $-3.8 \leq \log U \leq -0.9$ . For  $\log U = -1.2$ ,  $-0.9 \leq [\text{C}/\text{H}] \leq -0.6$ . This system is well modeled by a single-phase, photoionized medium.

#### 4.5. $z_{abs} = 0.09487$ : Partial Lyman Limit System

This system shows strong H I Lyman absorption from  $\text{Ly}\alpha$  to H I 914a (see Figure 9).  $\text{Ly}\epsilon$  is in the wings of Galactic  $\text{Ly}\beta$  absorption, and the higher-order Lyman lines H I 926 up to H I 914a fall in a region riddled with H<sub>2</sub> lines. Though the Lyman break  $\lambda 912$  is in a region of LiF 1A with low sensitivity,  $\log N_{\text{HI}}$  can be measured from the flux decrement at the limit. The optical depth  $\tau_{912} = \ln(f_{QSO}/f_{912}) = \sigma_{912}N_{\text{HI}}$ , where  $f_{QSO}$  ( $f_{912}$ ) is the flux redward (blueward) of the break and the cross section at the limit  $\sigma_{912} = 7.9 \times 10^{-18}$  cm<sup>-2</sup> (see Figure 10). We measure  $\log N_{\text{HI}} = 17.2 \pm 0.2$ , consistent with the COG value discussed below.

The majority of the Lyman series from  $\text{Ly}\alpha$  to H I 914a were used in the H I COG analysis:  $\log N_{\text{HI}} = 16.87^{+0.03}_{-0.03}$  and  $b = 30.7^{+0.5}_{-0.5}$  km s<sup>-1</sup> (see Figure 11). A single-component COG fits the data well, though this system has multi-components, as seen in the  $\text{Ly}\alpha$ , C III, and Si III line profiles.

C III and Si III are well-aligned with  $\text{Ly}\alpha$ . This system is the strongest C III absorber in the PKS1302–102 sight line  $\log N(\text{C}^{++}) > 13.9$ . A broad, well-aligned O VI doublet is detected with an  $W_r$  ratio of  $2.3 \pm 0.3$  and  $\log N(\text{O}^{+5}) = 14$ . Si II  $\lambda 1260$ , O I, C II, and the Si IV and C IV doublets are not detected at  $3\sigma$ .

For the CLOUDY models with  $\log N_{\text{HI}} = 16.75$ , the ionic ratios  $N(\text{C}^+)/N(\text{C}^{++})$  and  $N(\text{Si}^{++})/N(\text{Si}^{+3})$  set  $-3.5 \leq \log U \leq -2.1$  (see Figure 12). For  $\log U = -2.8$ , we derive  $-2.1 < [\text{C}/\text{H}] < -1.4$  and  $[\text{Si}/\text{H}] = -1.7$  (see Table 6). O VI is very broad, and this indicates at least a kinematically different phase from the C III and Si III absorption. Likely, O VI is thermally broadened, and we should consider the CLOUDY CIE models. The system could not be reasonably described by a single-phase CIE model since there would not be significant absorption of

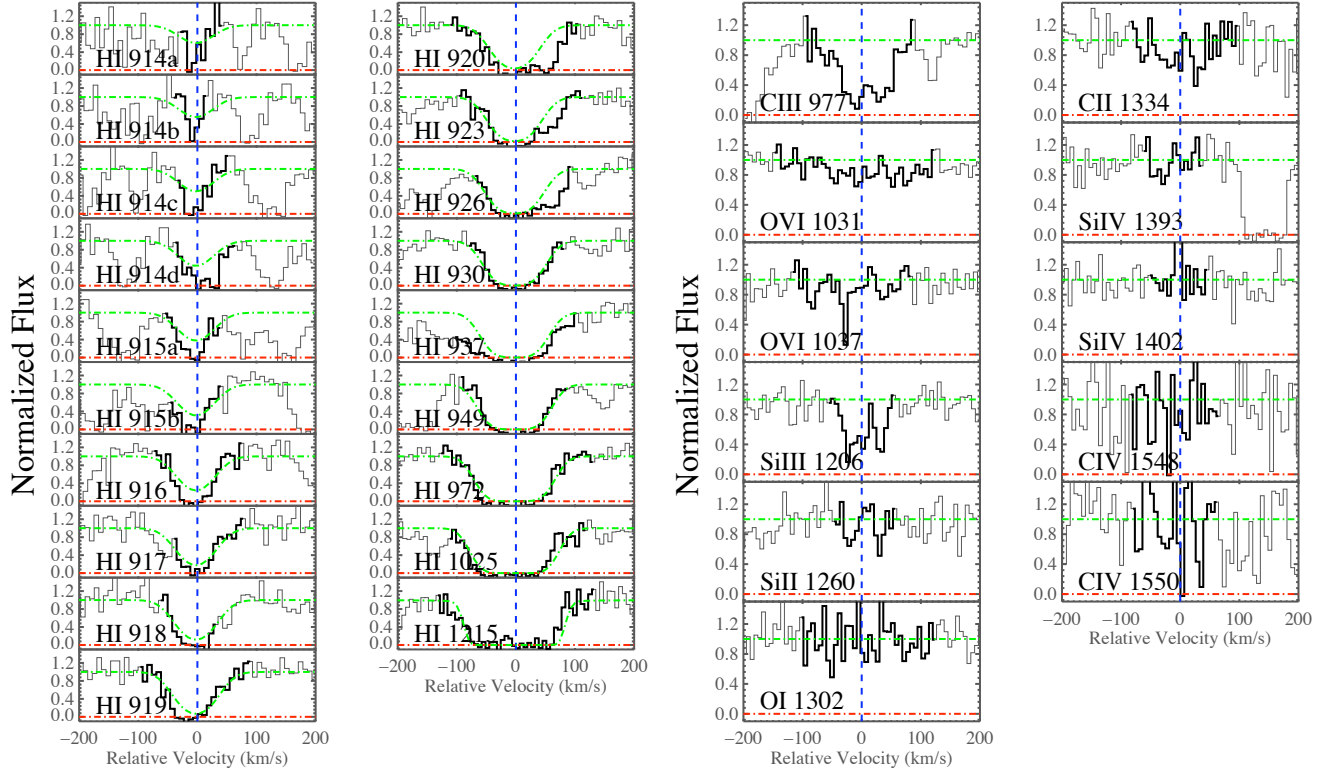


FIG. 9.— Velocity plot for the partial Lyman limit system at  $z_{abs} = 0.09487$  (see Figure 1 description). Ly $\epsilon$  lies in the wings the damped Galactic Ly $\beta$ , and the higher-order Lyman lines H I 914d, 916, 920, 923, and 926 are blended or coincident with H<sub>2</sub>. For H I 917 and 918, the H<sub>2</sub> blends, 1004.0 R(2) and 1005.4 P(2), respectively, are excluded from the  $W_r$  measure. This system was used to shift the *FUSE* channels onto the STIS wavelength solution. The Voigt profile centroid is fixed at  $z_{915a} = 0.09486$ . Ly $\alpha$ , C III, and Si III are well aligned, and they have similar, multi-component profiles. A broad O VI doublet is detected at  $>3\sigma$ . The  $W_r$  ratio of O VI 1031 to 1037 is  $2.3 \pm 0.3$ , in agreement with the predicted value for the unsaturated regime. Si II, O I, C II, and the Si IV and C IV doublets are not detected at  $3\sigma$ . (Note: the horizontal limits are from -200 to +200 km s<sup>-1</sup>.) Ly $\alpha$ , C III, and Si III are well aligned, and they have similar, multi-component profiles. A broad O VI doublet is detected at  $>3\sigma$ . The  $W_r$  ratio of O VI 1031 to 1037 is  $2.3 \pm 0.3$ , in agreement with the predicted value for the unsaturated regime. Si II, O I, C II, and the Si IV and C IV doublets are not detected at  $3\sigma$ .

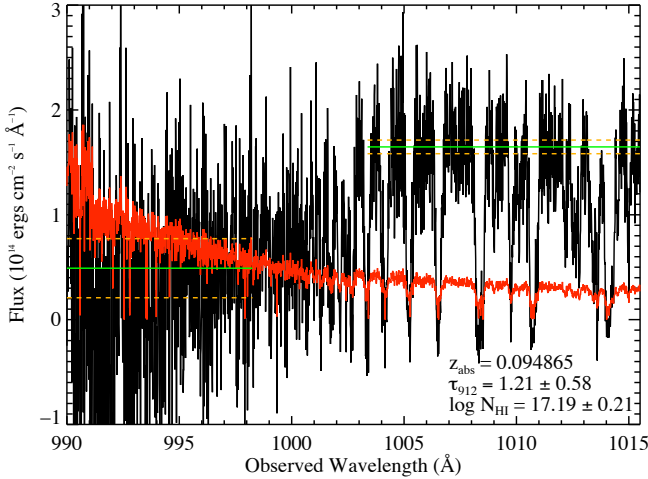


FIG. 10.— Lyman limit at  $z_{abs} = 0.09487$ . We show our fits and conservative error estimates (solid green and dashed orange lines, respectively) for the quasar continuum redward of the  $\lambda 912$  break and the flux blueward. From the flux decrement, we measure the optical depth at the limit and the H I column density. The red line is the error array of the spectrum. This portion of the spectrum is at the blue edge of Li I 1A, where the sensitivity decreases.

C III and O VI at one temperature without significant C IV absorption (see Figure 13). For CIE, the temperature limit  $T \geq 1.8 \times 10^5$ , set by  $N(C^{++})/N(O^{+5})$ , yields  $[O/H] > -2.6$  assuming the total  $N_{HI}$  value of this absorber, which is most likely dominated by the photoion-

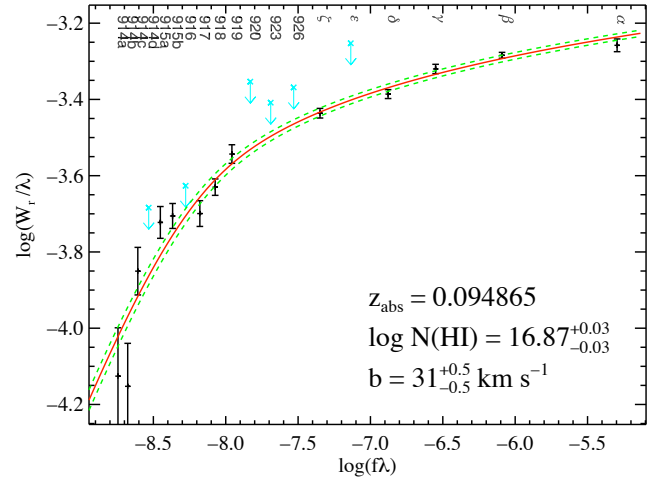


FIG. 11.— H I COG for  $z_{abs} = 0.09487$  (see Figure 2 description). This system is fit well by a single-component COG model despite Ly $\alpha$  having a multi-component line profile (see Figure 9).

ized phase.

The  $z_{abs} = 0.09487$  partial Lyman limit system is a metal-poor ( $-3 \lesssim [M/H] \lesssim -1$ ) and two-phased medium. C III and Si III are from one phase; they are narrow, multi-component features from a photoionized medium. The broad O VI indicates another phase that may either be photoionized or collisionally ionized.

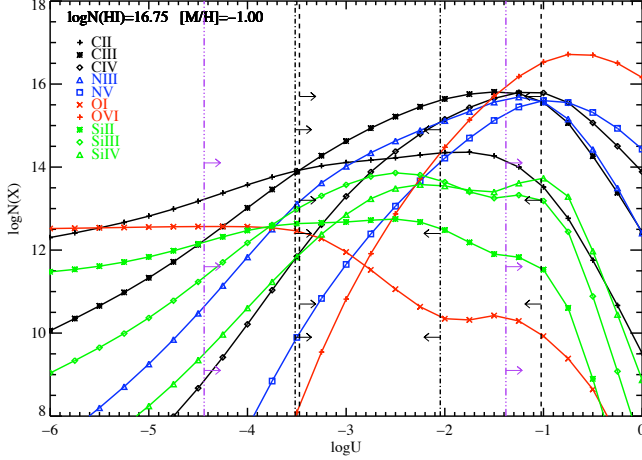


FIG. 12.— Column densities from CLOUDY photoionization model for  $z_{abs} = 0.09487$ . The model is parameterized by  $\log N_{\text{HI}} = 16.75$  and metallicity scaled to one-tenth solar abundance  $[M/H] = -1$ . The ionic ratios of the detected metal lines for  $z_{abs} = 0.09487$  constrain  $\log U$ :  $N(\text{C}^+)/N(\text{C}^{++})$  and  $N(\text{C}^{++})/N(\text{C}^{+3})$  (black dashed lines, left and right, respectively);  $N(\text{Si}^+)/N(\text{Si}^{++})$  and  $N(\text{Si}^{++})/N(\text{Si}^{+3})$  (black dash-dot lines, left and right, respectively); and  $N(\text{O}^0)/N(\text{C}^{++})$  and  $N(\text{C}^{++})/N(\text{O}^{+5})$  (purple dash-dot-dot-dot lines, from left to right).

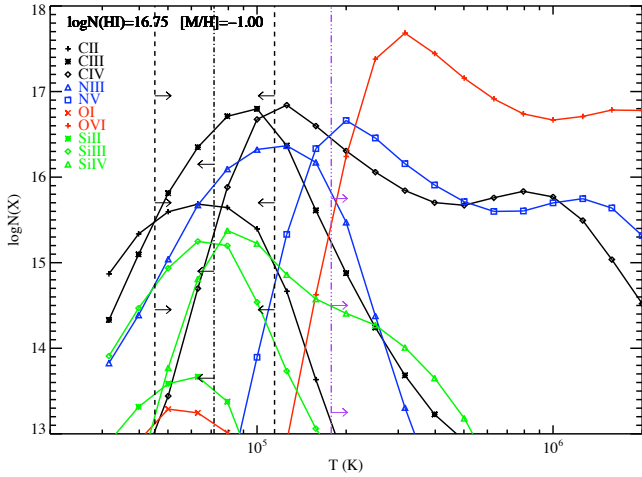


FIG. 13.— Column densities from CLOUDY collisional ionization equilibrium model for  $z_{abs} = 0.09487$ . The model is parameterized by  $\log N_{\text{HI}} = 16.75$  and  $[M/H] = -1$  (same as in Figure 12). The ionic ratios of detected metal lines for  $z_{abs} = 0.09487$  constrain the temperature:  $N(\text{C}^+)/N(\text{C}^{++})$  and  $N(\text{C}^{++})/N(\text{C}^{+3})$  (dashed lines, left and right, respectively);  $N(\text{Si}^+)/N(\text{Si}^{++})$  (dash-dot line); and  $N(\text{C}^{++})/N(\text{O}^{+5})$  (purple dash-dot-dot-dot line).

#### 4.6. $z_{abs} = 0.14529$ : C III

Although Ly $\alpha$  is as broad as that of the partial Lyman limit system discussed previously, the system at  $z_{abs} = 0.14529$  has a significantly lower  $N_{\text{HI}}$  value (see Figure 14). Ly $\alpha$ , Ly $\beta$ , and Ly $\gamma$  were used to fit the H I COG:  $\log N_{\text{HI}} = 15.37_{-0.03}^{+0.03}$  and  $b = 57_{-2}^{+2} \text{ km s}^{-1}$  (see Figure 15). Ly $\delta$  was excluded because it lies near the edge of LiF 2A; it deviates from the value predicted by the COG by  $>5\sigma$ . This discrepancy may also indicate that the system is multicomponent and poorly modeled by a single-component COG.

C III is well aligned with the broad Ly $\alpha$ , and

TABLE 6  
ELEMENTAL  
ABUNDANCES FOR  
ABSORBER AT  $z=0.09487$

Ion	$[X/H]$	$[X/C^{++}]$
C <sup>+</sup>	$< -1.38$	$< 0.72$
C <sup>++</sup>	$> -2.10$	$> 0.00$
C <sup>+3</sup>	$< -0.78$	$< 1.32$
O <sup>0</sup>	$< 1.50$	$< 3.60$
O <sup>+5</sup>	1.22	3.32
Si <sup>+</sup>	$< -1.05$	$< 1.05$
Si <sup>++</sup>	-1.74	0.36
Si <sup>+3</sup>	$< -1.29$	$< 0.82$

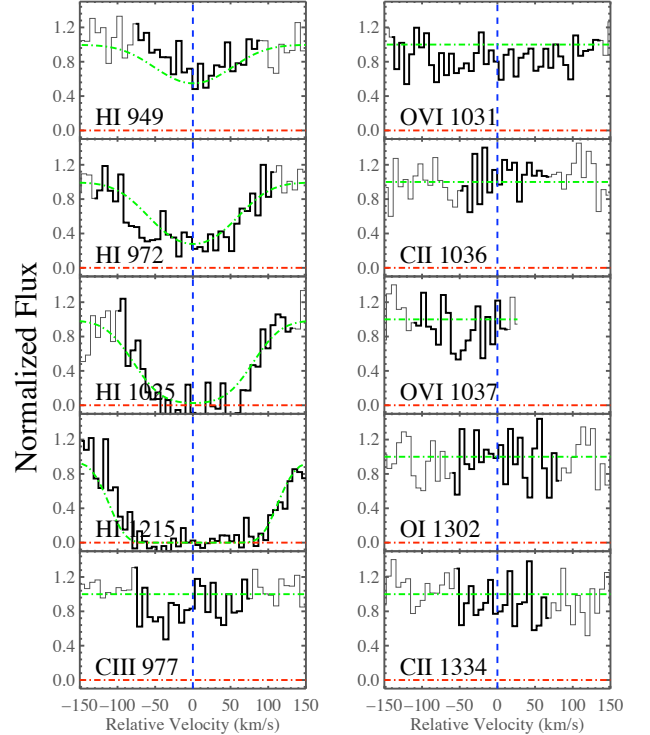


FIG. 14.— Velocity plot for  $z_{abs} = 0.14529$  (see Figure 1 description). Ly $\delta$  is near the edge of the LiF 2A spectrum. C III is a  $>6\sigma$  detection (see Table 3). Both C II lines and O I are not detected at  $>3\sigma$ . The O VI doublet is not a confirmed detection; O VI 1037 is at the edge of LiF 1B and in a noisy region of STIS. The Voigt profile centroid is fixed at  $z_{\beta} = 0.14530$ .

$\log N(\text{C}^{++}) = 13.2$  (see Table 3). A detection of the O VI doublet is not confirmed because O VI 1037 is at the edge of LiF 1B and in the low-sensitivity region of STIS. An upper limit is given from O VI 1031:  $\log N(\text{O}^{+5}) < 14.2$ . O I and C II are not detected at  $3\sigma$  significance.

In the CLOUDY model with  $\log N_{\text{HI}} = 15.25$ , the ionic ratios  $N(\text{C}^+)/N(\text{C}^{++})$  and  $N(\text{C}^+)/N(\text{O}^{+5})$  set  $-4.1 \leq \log U \leq [C/O] - 1.3$ . Assuming  $\log U = -1.8$ , the value predicted by Prochaska et al. (2004),  $[C/H] = -1.8$  and  $[O/H] < -0.5$  for  $[C/O] = 0$ . In the CLOUDY CIE model, the same ratios set  $7.8 \times 10^4 \leq T \leq 1.9 \times 10^5 \text{ K}$ . Assuming the width of H I is due purely to thermal broadening, then  $T = b^2 m / (2k) < 1.9 \times 10^5 \text{ K}$ , where  $m$  is the mass of hydrogen and  $k$  is the Boltzmann constant. For the upper  $T$  bound,  $[C/H] = -1.4$  and  $[O/H] < -1.2$ . This system can be modeled by a single-phase photoionized or collisionally-ionized medium.

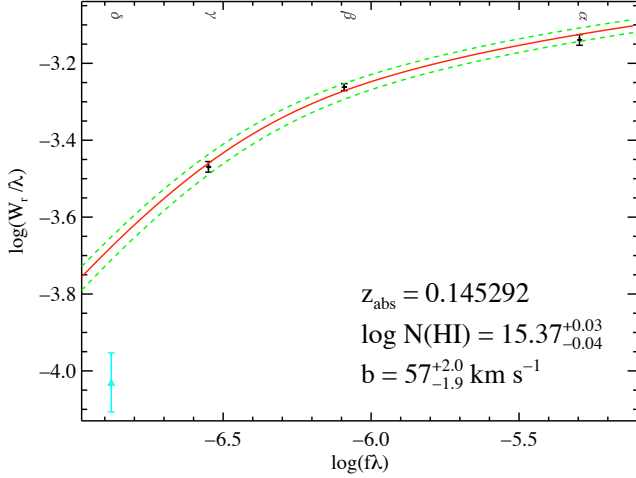


FIG. 15.— H I COG for  $z_{abs} = 0.14529$  (see Figure 2 description). The difference between the predicted and measured  $W_r$  of Ly $\delta$  is significant and suggests that H I is multi-component and poorly fit by this single-component COG.

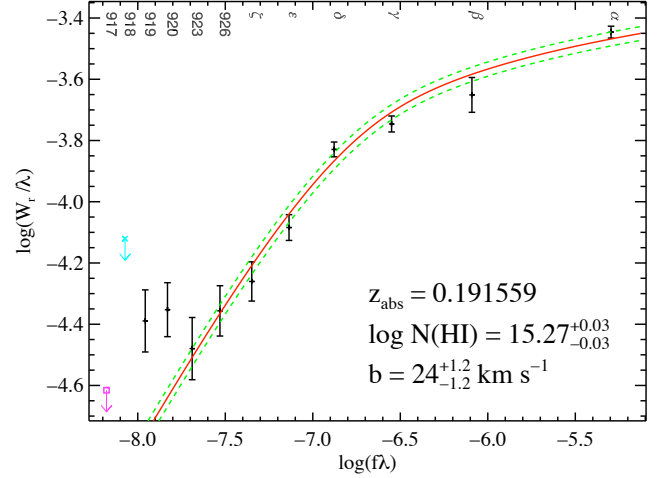


FIG. 17.— H I COG for  $z_{abs} = 0.19156$  (see Figure 2 description). H I 919 and 920 deviate  $< 3\sigma$  from the fit.

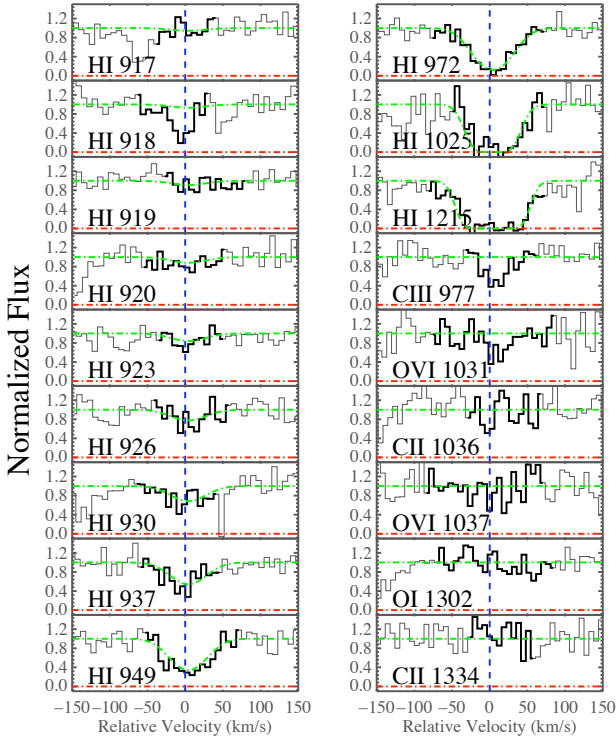


FIG. 16.— Velocity plot for  $z_{abs} = 0.19156$  (see Figure 1 description). H I 917, both C II lines, O I, and the O VI doublet are not detected at  $3\sigma$ . H I 918 is blended with H<sub>2</sub> 1094.0 P(1). The Voigt profile centroid is fixed at  $z_{\delta} = 0.19158$ .

#### 4.7. $z_{abs} = 0.19156$ : C III

This system is another strong Lyman absorber with C III well aligned with Ly $\alpha$  (see Figure 16). The H I COG is consistent from Ly $\alpha$  to H I 917:  $\log N_{\text{HI}} = 15.27^{+0.03}_{-0.03}$  and  $b = 23^{+1.2}_{-1.2} \text{ km s}^{-1}$ . H I 917, the O VI doublet, O I, and both C II lines are not detected at  $3\sigma$ . H I 918 is blended with H<sub>2</sub> 1094.0 P(1) (see Figure 17).

This system does not have strong C III absorption:  $\log N(\text{C}^{++}) = 13.1$  (see Table 3). In the CLOUDY models for  $\log N_{\text{HI}} = 15.25$ , the ionic ratios  $N(\text{C}^+)/N(\text{C}^{++})$  and  $N(\text{C}^+)/N(\text{O}^{+5})$  constrain  $-4 \geq \log U \leq [\text{C}/\text{O}] - 1.3$ .

TABLE 7  
LY $\alpha$  ABSORBERS SUMMARY

$\lambda_{obs}$ (Å)	$z_{abs}$	$W_r$ (mÅ)	$\log N_{\text{HI}}^a$	$b^a$ (km s <sup>-1</sup> )
$\log N_{\text{HI}} \geq 14.0^b$				
1335.980	0.09897	357 ± 16	14.23 <sup>+0.05</sup> <sub>-0.05</sub> <sup>c</sup>	34 <sup>+3.5</sup> <sub>-3.0</sub>
1421.555	0.16936	184 ± 27	14.04 <sup>+0.19</sup> <sub>-0.27</sub> <sup>c</sup>	16 <sup>+10.0</sup> <sub>-3.6</sub>
1449.595	0.19242	225 ± 17	14.12 <sup>+0.15</sup> <sub>-0.21</sub> <sup>c</sup>	19 <sup>+7.0</sup> <sub>-2.8</sub>
1489.828	0.22552	274 ± 27	> 14.02	...
1518.098	0.24877	298 ± 26	14.23 <sup>+0.10</sup> <sub>-0.11</sub>	26 <sup>+5.3</sup> <sub>-3.8</sub>
1522.207	0.25215	423 ± 25	14.77 <sup>+0.18</sup> <sub>-0.12</sub>	29 <sup>+3.2</sup> <sub>-3.2</sub>
$\log N_{\text{HI}} < 14.0^b$				
1269.706	0.04445	117 ± 23	13.53 ± 0.09	...
1271.840	0.04621	56 ± 18	13.23 ± 0.15	...
1272.318	0.04660	243 ± 26	13.99 <sup>+0.13</sup> <sub>-0.15</sub>	26 <sup>+14.9</sup> <sub>-6.0</sub>
1287.017	0.05869	71 ± 21	13.36 ± 0.11	...
1288.212	0.05967	55 ± 17	13.25 ± 0.14	...
1365.526	0.12327	202 ± 26	13.82 ± 0.11	...
1450.227	0.19294	229 ± 17	13.99 <sup>+0.20</sup> <sub>-0.26</sub> <sup>c</sup>	23 <sup>+34.9</sup> <sub>-4.6</sub>
1523.129	0.25291	232 ± 24	> 13.94	...
1524.592	0.25412	257 ± 33	> 13.95	...

<sup>a</sup> Where  $b$  not given,  $\log N_{\text{HI}}$  from the AODM and is typically a lower limit. Otherwise,  $\log N_{\text{HI}}$  and  $b$  calculated from COG analysis where at least one other Lyman line also detected. <sup>b</sup> Strong Ly $\alpha$  features have  $\log N_{\text{HI}} \geq 14.0$ . <sup>c</sup> COG analysis notes: for  $z_{abs} = 0.09897$  Ly $\alpha$  blended with G C II\* 1335;  $z_{abs} = 0.16936$  Ly $\beta$  blended with G N I 1199; for  $z_{abs} = 0.19242$  Ly $\beta$   $< 3\sigma$ , Ly $\alpha$ , Ly $\gamma$  COG; for  $z_{abs} = 0.19294$  Ly $\beta$   $< 3\sigma$ , Ly $\alpha$ , Ly $\gamma$  COG

For  $\log U = -1.8$ ,  $[\text{C}/\text{H}] = -1.9$  and  $[\text{O}/\text{H}] \leq -0.7$  for  $[\text{C}/\text{O}] = 0$ . This system can be described as a single-phase photoionized medium.

#### 5. STRONG Ly $\alpha$ ABSORBERS WITHOUT METALS

In addition to the seven metal-line systems described above, we identified 16 Ly $\alpha$  features detected at  $> 3\sigma$  significance (see Table 7). There are seven Ly $\alpha$  lines with  $\log N_{\text{HI}} \geq 14$  that we identify as strong. Given the absence of metal-line absorption, the identification of these lines as Ly $\alpha$  should be considered less secure. However

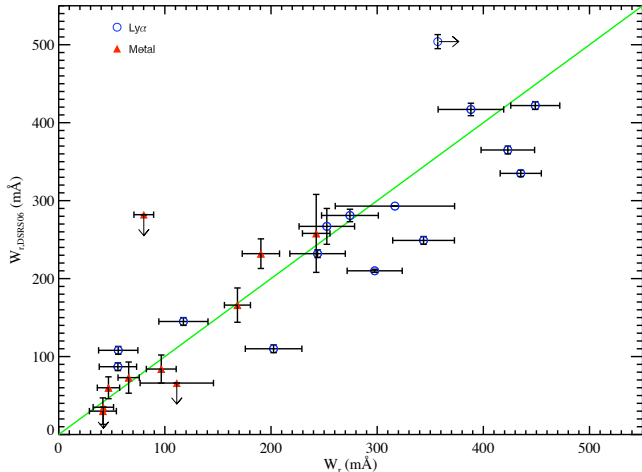


FIG. 18.— Comparison of rest equivalent widths from our analysis with Danforth et al. (2006). The DRS06 values are plotted over the values measured in the current paper, and the one-to-one relation is shown (solid green line).

three of the strong Ly $\alpha$  lines show corresponding Ly $\beta$  absorption at  $> 3\sigma$  significance, which lends credibility to our identification. In Table 7, we quote either the AODM column density or  $\log N_{\text{HI}}$  and  $b$  from the COG analysis when there is at least one other Lyman line detected. The  $\log N_{\text{HI}}$  values from the AODM are lower limits when Ly $\alpha$  is saturated.

The Ly $\alpha$  absorbers at  $z_{\text{abs}} = 0.19242$  and  $0.19294$  are within  $\delta v_{\text{abs}} < 350 \text{ km s}^{-1}$  of the metal-line system at  $z_{\text{abs}} = 0.19156$ . Ly $\alpha$  at  $z_{\text{abs}} = 0.22449$  and  $0.22552$  are within  $\delta v_{\text{abs}} < 250 \text{ km s}^{-1}$  of each other. The implications of these close systems will be discussed in the following galaxy section.

The Ly $\alpha$  absorber at  $z_{\text{abs}} = 0.25215$  has larger  $\log N_{\text{HI}}$  than the the O VI system at  $z_{\text{abs}} = 0.06468$ . As mentioned previously, metal-line absorption roughly scales with  $\log N_{\text{HI}}$ ; the  $z_{\text{abs}} = 0.25215$  system should show some metal-line absorption since  $z_{\text{abs}} = 0.06468$  did. These systems appear to be at the edge of our ability to detect metal-line absorbers.

## 6. COMPARISONS WITH PREVIOUS ANALYSIS

The STIS dataset (PI: M. Lemoine) was acquired to measure an intergalactic D/H value from the  $z = 0.095$  partial Lyman limit system. Unexpected line-blending has apparently precluded such an analysis (Lemoine, priv. comm.) and the data was not studied for this purpose. PKS1302–102 was included, however, in the compilation of Danforth et al. (2006) who studied Ly $\alpha$ , Ly $\beta$ , O VI, and C III lines along 31 AGN sightlines at  $z < 0.3$ . We have compared our results against DRS06 to search for systematic effects related to different procedures of data reduction and analysis. In particular, we have derived equivalent widths differently than DRS06; our analysis adopts values from a simple boxcar summation whereas DRS06 implemented line-profile fits using the VPFIT software package.

Figure 18 presents a comparison of the rest equivalent width ( $W_r$ ) measurements of DRS06 against our values for Ly $\alpha$  and metal-line transitions. We find that the two sets of measurements are in good agreement for  $W_r$  values of metal-line transitions. Similarly, there is relatively good agreement between the two studies for Ly $\alpha$  lines at

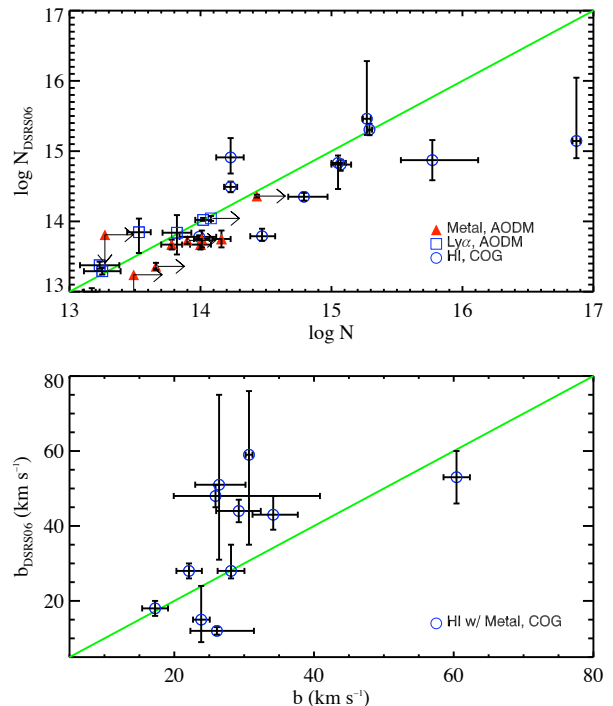


FIG. 19.— Comparison of column densities and Doppler parameters reported by DRS06 against those from our analysis. The categories denoted by color and symbol refer to the current work. The HI COG analysis  $\log N$  and  $b$  are blue circles, and the AODM  $\log N$  are triangles, where blue is for Ly $\alpha$ -only systems and red for metal lines (*i.e.*, C III and O VI). For the top row, the blue points are for Ly $\alpha$   $W_r$ , and the upper left panel is focused on the lower  $W_r$  region of its neighbor plot. DRS06 use COG concordance plots, Voigt profile fits, and/or the AODM to measure  $\log N_{\text{DRS06}}$  and  $b_{\text{DRS06}}$ , typically assuming a single component. From  $\log N_{\text{DRS06}}$  and  $b_{\text{DRS06}}$ , they measure  $W_{r, \text{DRS06}}$ . They tend to underestimate  $W_{r, \text{DRS06}}$  compared to our values, which are a simple sum of the absorbed flux and include unresolved components. We generally agree with  $\log N_{\text{DRS06}}$  because the sum of potential components does not greatly affect the total column density. On the other hand, unresolved components tend to increase  $b_{\text{DRS06}}$  compared our values, as discussed in DRS06.

low rest equivalent widths ( $W_r < 300 \text{ mÅ}$ ). The only notable difference is that the DRS06 rest equivalent width errors  $\sigma(W_r)$  for the Ly $\alpha$  lines are systematically lower than our values; DRS06 report  $\sigma(W_r) \leq 5 \text{ mÅ}$  for the majority of their lines. While line-profile fitting techniques can recover more precise measurements of the equivalent width than a boxcar summation, we contend that a 5 mÅ error cannot be achieved from this dataset ( $S/N \approx 3$  per pixel). Even for strong lines where one might be justified in assuming the core has zero flux with zero uncertainty, the wings of the line-profile have equivalent width errors of greater than 10 mÅ. We can only speculate on the implications of adopting very small errors on  $W_r$  for Ly $\alpha$  transitions. DRS06 performed concordance COG analysis of  $N_{\text{HI}}$  and  $b$  values in a similar manner as the analysis presented here. Because the Ly $\alpha$  line has the largest  $W_r$  value in the Lyman series, adopting a very small uncertainty will drive the COG analysis to best model the Ly $\alpha$  transition. In particular, this will imply  $b_{\text{COG}} = b_{\text{Ly}\alpha}$  which DRS06 emphasize generally overestimates the true Doppler parameter of the ‘cloud’ dominating the optical depth. We will return to this point below.

There are more serious discrepancies between our re-

sults and DSRS06 for stronger Ly $\alpha$  lines ( $W_r > 300$  mÅ). First, we identify five Ly $\alpha$  lines with  $\log N_{\text{HI}} > 13.9$  that DSRS06 have not, at  $z_{\text{abs}} = 0.16936, 0.19242, 0.19294, 0.25291,$  and  $0.25412$ . The  $z_{\text{abs}} = 0.16936$  Ly $\alpha$  is a multi-component system with Ly $\beta$  lost in Galactic N I. The other four lines are line-center saturated (or nearly so), but Ly $\beta$  is not detected at  $3\sigma$ . These features are not Galactic lines nor misidentified metal lines from other intervening systems. Although DSRS06 detect other strong Ly $\alpha$  lines without Ly $\beta$  absorption, these lines were not reported in their survey. Second, we have derived systematically larger  $W_r$  values for strong Ly $\alpha$  lines. Most notable are the five Ly $\alpha$  lines in Figure 18 with  $W_r$  about 100 mÅ greater than the  $W_r$  values reported by DSRS06. The majority of the discrepancy is probably due to these features being multi-component; we quote the total  $W_r$  of the feature whereas DSRS06 generally only report the strongest single component. We find similar differences when comparing the DSRS06 results for PKS0405–123 against the results reported in Prochaska et al. (2004).

We also compare the column densities and Doppler parameter values for absorption lines analyzed by DSRS06 (see Figure 19). The metal-line column densities are considered first. In contrast to the equivalent width measurements for these transitions, we find that our values are systematically larger than those reported by DSRS06. Most worrisome is that we report several lower limits to the column density of C III because the line is clearly saturated in the FUSE observations whereas DSRS06 report not a single lower limit. For example, we report  $\log N(\text{C}^{++}) > 13.9$  for the C III transition in the  $z = 0.09487$  absorber whereas DSRS06 report  $\log N(\text{C}^{++}) = 13.73 \pm 0.05$ . The differences in O VI column densities are  $< 0.3$  dex, and probably due to continuum placement. The broad, shallow O VI detection at  $z_{\text{abs}} = 0.09487$  differs by 0.3 dex whereas the stronger  $z_{\text{abs}} = 0.04226$  feature differs only by 0.1 dex.

Regarding the H I column densities, we note trends similar to those for the  $W_r$  values: at low column densities there is good agreement between the two analyses, but at larger  $N_{\text{HI}}$  our values are systematically larger. The difference is most acute for the two systems at  $\log N_{\text{HI}} > 15.5$ :  $z_{\text{abs}} = 0.00442$  and  $0.09487$ . As mentioned in § 4.1, DSRS06 use a profile fit to  $z_{\text{abs}} = 0.00442$  Ly $\alpha$ , which falls in the Galactic damped Ly $\alpha$  profile, to determine  $N_{\text{HI}}$ . Our COG analysis includes Ly $\beta$ , which is the only feature of the system in a good region of the spectra. The difference for  $z_{\text{abs}} = 0.09487$  is due to DSRS06 only including Ly $\alpha$  through H I 926 in their concordance COG analysis. For this system, the higher-order H I Lyman lines are most important for measuring the  $N_{\text{HI}}$  value.

Finally, we have compared the Doppler parameter values from the two analyses (Figure 19; lower panel). At low  $b$  values, we find reasonable agreement, but at moderate values our results are systematically lower than the values reported by DSRS06. We suspect the discrepancy is related to the very small errors adopted for their Ly $\alpha$  equivalent widths (Figure 18). In this case, a COG analysis will yield a Doppler parameter which better describes Ly $\alpha$  and, as DSRS06 emphasize,  $b_{\text{Ly}\alpha}$  is systematically larger than  $b_{\text{COG}}$ . Because DSRS06 generally adopt equivalent values from the literature (e.g. Penton et al. 2004), it is possible that this systematic

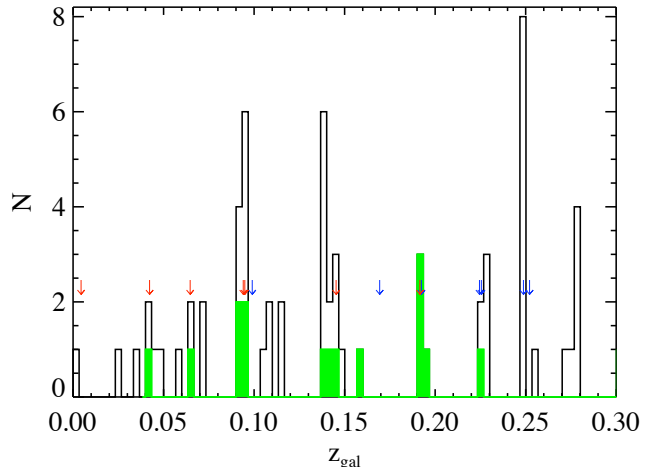


FIG. 20.— Histogram of 64 galaxies with  $z_{\text{gal}} \leq 0.3$  in PKS1302–102 field, binned to  $1000 \text{ km s}^{-1}$  (open). The solid (green) histogram is galaxies within  $5'$ , 90% complete to  $R \approx 19.5$ . The arrows indicate the redshifts of the seven metal-line systems (red) and the seven strong Ly $\alpha$  absorbers (blue) (see Table 7). There are groups of absorbers with  $\delta v_{\text{abs}} < 500 \text{ km s}^{-1}$  and with nearby galaxies that may be large-scale filaments at  $z_{\text{abs}} \approx 0.094, 0.192,$  and  $0.225$ .

effect is only present in the few sightlines analyzed by DSRS06 (e.g., PKS1302–102, PKS0405–123). We also note that the larger  $b$  values likely lead to a systematic underestimate of  $N_{\text{HI}}$  which explains at least part of the offset of their values from our results for  $\log N_{\text{HI}} > 14$ .

## 7. GALAXY SURVEY

A number of studies have examined the relationship between galaxies and absorption-line systems at  $z \lesssim 0.1$ . Regarding metal-line systems, the majority of recent analyses can be characterized as a detailed study of a single or few absorbers (e.g. Stocke et al. 2004; Jenkins et al. 2005; Tripp et al. 2006a), an analysis of a complete sightline and its surrounding galaxies (Sembach et al. 2004b; Prochaska et al. 2006), or a survey comprising multiple fields and absorbers (Stocke et al. 2006). These studies have examined metal-line systems associated with a diverse set of ions ( $\text{Si}^+, \text{C}^+, \text{O}^0, \text{O}^{+5}$ ), metallicities, and H I column densities. Furthermore, the galaxy surveys have a wide range of magnitude limits and field-of-view areas. Not surprisingly, a range of conclusions have been drawn regarding the association of galaxies and absorbers including: (i) a physical association of the gas with individual galactic halos (Chen & Prochaska 2000), (ii) outflows from dwarf galaxies (Stocke et al. 2004), and large-scale (e.g. filamentary) structures (Stocke et al. 2006; Tripp et al. 2006a). Indeed, all of these may contribute to metal-line systems, presumably with a dependence on the metallicity, ionization state, and column density of the gas. Other analyses begin with a well-defined galaxy survey and search for absorption associated with galaxies at small impact parameters to the sightline (Lanzetta et al. 1995; Chen et al. 2001a,b). These authors conclude that the presence of a galaxy within  $\approx 200 \text{ kpc}$  of a quasar sightline results in a high probability of showing coincident Ly $\alpha$  and C IV absorption.

Our analysis of PKS1302–102 has identified seven metal-line systems showing a diverse set of character-

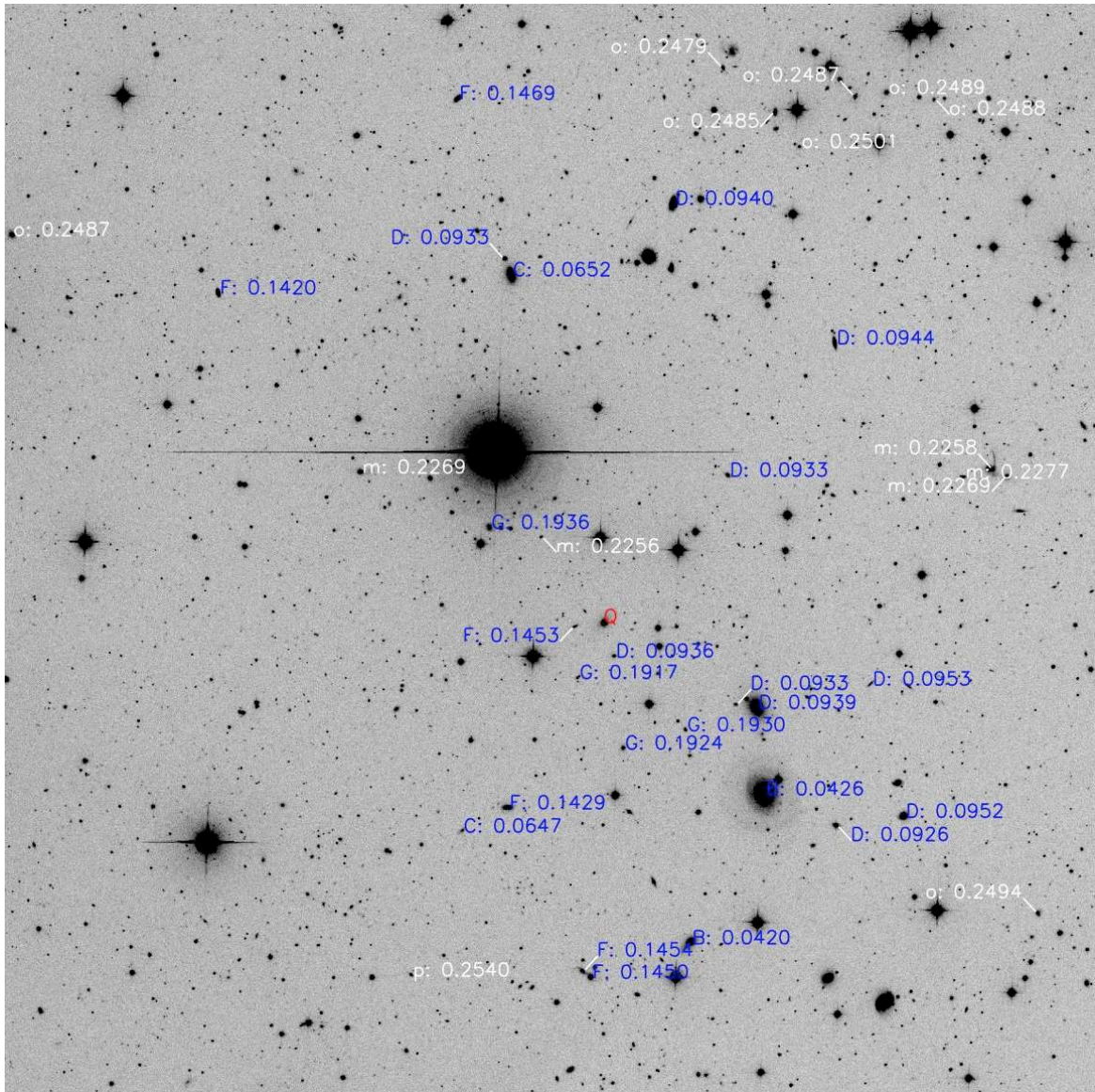


FIG. 21.— Galaxies with  $|\delta v_{\text{gal}}| \leq 1000 \text{ km s}^{-1}$  from metal-line systems and strong Ly $\alpha$  absorbers. The former have (blue) capital letters indicating the system they neighbor, while the latter have (white) lower case letters. The systems at  $z_{\text{abs}} = 0.0940$  and  $0.09487$  have most all neighboring galaxies in common; they are not labeled twice. The O VI systems are at  $z_{\text{abs}} = 0.04226$ ,  $0.06468$ , and  $0.09487$  (B, C, and D, respectively). Aside from  $z_{\text{abs}} = 0.14529$  (F), the metal-line systems are more likely probing the intra-group medium. (North is up, and east is left. There are about a dozen galaxies in the southeast corner that are either at higher redshift than PKS1302–102 or not within  $1000 \text{ km s}^{-1}$  of an intervening system.) The image is about  $20'$  on a side.

istics, and we might expect, therefore, them to arise in a range of galactic environments. We have obtained spectra of galaxies in the field surrounding PKS1302–102 using the WFCCD camera on the  $100''$  Dupont telescope at Las Campanas Observatory during UT 2001-04-16–2001-04-20. We refer the reader to Prochaska et al. (2006) for details of the imaging and spectral data reduction and analysis procedures. The survey of the PKS1302–102 field is 95% complete within  $5'$  and 70% within  $10'$  to the limiting magnitude  $R \approx 19.5$ . We have redshift information for 82 galaxies in the PKS1302–102 field, 64 of which are at  $z_{\text{gal}} < z_{\text{QSO}}$ . At the highest redshifts  $z_{\text{abs}} \approx 0.25$ , the survey covers a physical radius of  $\approx 3 \text{ Mpc}$  but not to faint intrinsic magnitudes ( $L \approx L_*$ ).<sup>13</sup> For the lowest redshift absorbers ( $z < 0.02$ ), we do not have the coverage to comment on large-scale

structures ( $\rho \approx 1\text{--}3 h_{75}^{-1} \text{ Mpc}$ ) as in *e.g.*, Penton et al. (2002) and Prochaska et al. (2004). For example, the field-of-view covers only  $\rho \lesssim 25 \text{ kpc}$  around the C III system  $z_{\text{abs}} = 0.00442$ , an absorber that is likely affiliated with the Virgo cluster.

Table 10 lists<sup>14</sup> the galaxies associated with the IGM systems by  $\delta v_{\text{gal}} \equiv c(z_{\text{abs}} - z_{\text{gal}})/(1 + z_{\text{abs}}) \leq 1000 \text{ km s}^{-1}$ . The velocity constraint comfortably covers the peculiar velocities expected for large-scale structures. In Figure 20 we show a histogram of the galaxy redshifts for the field surrounding PKS1302–102 and Figure 22 the impact distribution of galaxies with  $|\delta v_{\text{gal}}| < 1000 \text{ km s}^{-1}$  from a metal-line system. Although an ex-

<sup>13</sup> In this paper, we assume a Hubble constant  $H_0 = 75 h_{75} \text{ km s}^{-1} \text{ Mpc}^{-1}$  and the absolute magnitude for  $L_*$  at  $z = 0$  is  $M_R = -21.04$  (Blanton et al. 2003). This value is one magnitude fainter than the value used in Prochaska et al. (2006).

<sup>14</sup> See also <http://www.ucolick.org/~xavier/WFCCDOVI/>

<sup>13</sup> In this paper, we assume a Hubble constant  $H_0 =$

TABLE 8  
OBJECT SUMMARY

ID	RA	DEC	$R$ (mag)	S/G <sup>a</sup>	Area ( $\square''$ )	flag <sup>b</sup>	$z$
4	13:04:56.0	-10:29:18	18.11 ± 0.02	0.09	6.8	7	0.27252
5	13:04:54.6	-10:39:58	17.89 ± 0.01	0.13	4.6	7	0.04576
107	13:06:21.4	-10:30:37	17.29 ± 0.01	0.25	7.3	7	0.10819
152	13:06:20.7	-10:27:53	17.98 ± 0.01	0.18	4.3	7	0.11608
171	13:06:19.5	-10:34:42	17.34 ± 0.01	0.22	4.2	7	0.13839
179	13:06:20.0	-10:26:11	17.96 ± 0.02	0.01	6.1	7	0.24866
234	13:06:17.0	-10:37:51	18.94 ± 0.03	0.89	4.2	7	0.35805
306	13:06:13.4	-10:44:51	18.57 ± 0.02	0.98	4.5	7	0.00000
329	13:06:15.4	-10:27:22	18.70 ± 0.02	0.13	4.9	7	0.36601
768	13:06:03.8	-10:27:12	17.58 ± 0.01	0.12	6.0	7	0.14202

NOTE. — [The complete version of this table is in the electronic edition of the Journal. The printed edition contains only a sample.]

<sup>a</sup> Star/galaxy classifier calculated by SExtractor. Values near unity indicate a stellar-like point-spread function. <sup>b</sup> This binary flag has the following code: 1: Photometry; 2: Spectrum taken; 4= Redshift determined.

act comparison of galaxy-absorber correlations cannot be performed between systems because the survey varies in field-of-view and depth with redshift, it is evident that the metal-line systems arise in a diverse set of galactic environments. For example, the partial LLS at  $z = 0.0948$  is associated with a group of galaxies and quite likely is found within the halo of a  $L \approx 0.2 L_*$  galaxy at  $\rho \approx 65 h_{75}^{-1}$  kpc. In contrast, the O VI absorber at  $z = 0.0646$  is at least  $300 h_{75}^{-1}$  kpc away from any galaxy with  $L > 0.01 L_*$  and one identifies no obvious large scale-structure at this redshift. Let us now turn to discuss a few of these absorbers in greater detail.

There are three groups of absorbers with  $|\delta v_{\text{abs}}| < 500 \text{ km s}^{-1}$  at  $z_{\text{abs}} \approx 0.094, 0.192,$  and  $0.225$ . These groups may represent filamentary structures where the H I absorption (and metal-line absorption, in the case of  $z_{\text{abs}} \approx 0.094$  and  $0.192$ ) arises in the gas between the galaxies populating this large-scale structure (Bowen et al. 2002). The  $z_{\text{abs}} \approx 0.094$  group has ten detected galaxies with  $65 < \rho < 800 h_{75}^{-1}$  kpc and  $0.1 < L/L_* < 6$ . The brightest galaxy is at  $\delta v_{\text{gal}} = -257 \text{ km s}^{-1}$  from the partial Lyman-limit system  $z_{\text{abs}} = 0.09487$ , with  $\rho = 331 h_{75}^{-1}$  kpc. Both absorption systems near  $z_{\text{abs}} \approx 0.094$  have C III absorption, and the partial LLS has Si III and a broad O VI doublet. Chen et al. (2001a) have found that C IV absorption is strongly correlated with galaxies with  $\delta v_{\text{gal}} < 250 \text{ km s}^{-1}$  and  $\rho < 100 h_{75}^{-1}$  kpc. We have searched for such absorption associated with the galaxy at  $z = 0.09358$  with  $\rho = 65 h_{75}^{-1}$  kpc but unfortunately this places the doublet in the high-wavelength, low-sensitivity end of the STIS E140M spectrum. We can place an upper limit on the absorption:  $\log N(\text{C}^{+3}) < 14.1$ . Given the small impact parameter of this galaxy to the PKS1302-102 sightline, we tentatively associate this galaxy with the partial LLS at  $z = 0.09487$ . This association is challenged by the observed velocity offset  $\delta v_{\text{gal}} = -352 \text{ km s}^{-1}$ ; an association would require the gas to have a large inflow/outflow.

The group at  $z_{\text{abs}} \approx 0.192$  has a strong H I Lyman absorber with C III absorption and two Ly $\alpha$  systems with  $\log N_{\text{HI}} > 13.9$ . There are four detected galaxies in this group, with  $200 < \rho < 520 h_{75}^{-1}$  kpc and  $0.4 < L/L_* < 2.5$ . In the  $z_{\text{abs}} \approx 0.225$  group, there

are five bright ( $L > 0.7 L_*$ ) galaxies detected in the field with all but one at  $\rho > 1 h_{75}^{-1}$  Mpc. There are very few galaxies in the survey around the remaining metal-line systems at  $z_{\text{abs}} = 0.04226, 0.06468,$  and  $0.14529$ . The O VI systems at  $z_{\text{abs}} = 0.04226$  and  $0.06468$  each have two galaxies with  $|\delta v_{\text{gal}}| < 160 \text{ km s}^{-1}$  and  $200 < \rho < 500 h_{75}^{-1}$  kpc. At these redshifts, the survey is 100% within 200 kpc ( $2'$ ) to  $L = 0.01 L_*$  and  $0.03 L_*$ , respectively ( $R = 20$  mag). For the  $z_{\text{abs}} = 0.06468$  system, the fainter galaxy ( $L \approx 0.05 L_*$ ) is closer in  $\delta v_{\text{gal}}$  and impact parameter, while the opposite is true for the other O VI absorber. In addition, the two galaxies around  $z_{\text{abs}} = 0.06468$  have larger  $\rho$  than the galaxies near  $z_{\text{abs}} = 0.04226$ . Since the  $z_{\text{abs}} = 0.06468$  O VI system has lower  $\log N_{\text{HI}}$  and  $\log N(\text{O}^{+5})$ , it may probe the extended halos of the nearby galaxies. The  $z_{\text{abs}} = 0.04226$  system, with O VI and C III, probably probes a multi-phase medium closer to the galaxies. Stocke et al. (2006) report that O VI systems with no C III absorption have larger nearest-galaxy distances than systems with both lines detected.

There are four galaxies surrounding the  $z_{\text{abs}} = 0.14529$  absorber with  $\delta v_{\text{gal}} < 500 \text{ km s}^{-1}$  and  $0.4 < L/L_* < 2.5$ , suggesting the gas arises in an intra-group medium (Mulchaey et al. 1996). However, one of these galaxies has a very small velocity offset and impact parameter ( $\delta v_{\text{gal}} = 2 \text{ km s}^{-1}$  and  $\rho = 80 h_{75}^{-1}$  kpc) and may host the broad H I and C III absorption. As for the other strong Ly $\alpha$  absorbers, there are surrounding galaxies with  $\delta v_{\text{gal}} < 1000 \text{ km s}^{-1}$ , except for  $z_{\text{abs}} = 0.12323$  and  $0.1694$ . However, no one bright and close galaxy appears as the source of the gas. The absorbers are likely probes of faint galaxy groups. The  $z_{\text{abs}} = 0.12323$  and  $0.16936$  Ly $\alpha$  absorbers are obviously multi-component features with no galaxies with  $\delta v_{\text{gal}} < 1000 \text{ km s}^{-1}$  and brighter than  $R = 19.5$  mag.

It is illustrative to compare the galaxy-absorber connection by examining the properties of the ‘nearest’ galaxy to each absorber and a characteristic of the large-scale structure. Before proceeding, however, we wish to caution that the nearest galaxy in this context corresponds to the galaxy with smallest impact parameter that (i) has  $|\delta v_{\text{gal}}| < 1000 \text{ km s}^{-1}$  and (ii) is brighter

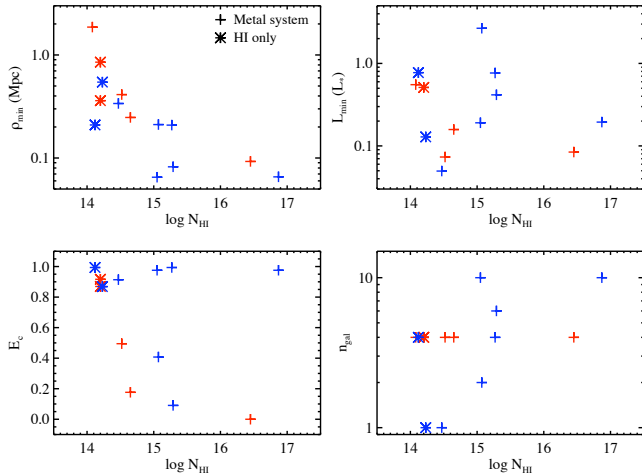


FIG. 22.— Impact parameter ( $\rho_{min}$ ), luminosity ( $L_{min}$ ), and spectral coefficient ( $E_C$ ) of the closest galaxy with  $L > 0.1 L_*$ ,  $\rho < 5$  Mpc, and  $|\delta v_{gal}| < 1000 \text{ km s}^{-1}$  for the absorbers with  $N_{\text{HI}} > 10^{14} \text{ cm}^{-2}$  at  $z_{abs} < 0.2$  along the sightlines to PKS0405–123 (red) and PKS1302–102 (blue). The point types distinguish between metal-line systems (plus signs) and absorbers that only show Ly $\alpha$  absorption (asterisks). There appears to be a trend toward lower  $\rho_{min}$  values for higher  $N_{\text{HI}}$  value of the absorbers. (Note: in the current work, the absolute magnitude for  $L_*$  at  $z = 0$  is one magnitude fainter than that used in Prochaska et al. (2006).)

than the magnitude limit. In many cases, there may be no direct physical association between the galaxy and the absorber. Figure 22 presents the impact parameter  $\rho_{min}$ , luminosity  $L_{min}$ , and spectral coefficient  $E_C$  of the galaxy at closest impact parameter to all of the absorbers with  $N_{\text{HI}} > 10^{14} \text{ cm}^{-2}$  along the sightlines to PKS0405–123 (Prochaska et al. 2004) and PKS1302–102 (this paper). In addition, the lower-right panel shows the number of galaxies with  $L > 0.1 L_*$ ,  $\rho < 5$  Mpc, and  $|\delta v_{gal}| < 1000 \text{ km s}^{-1}$  with respect to the absorber. In terms of the impact parameter, one notes a qualitative trend of decreasing  $\rho_{min}$  with increasing  $N_{\text{HI}}$  that suggests a physical association between individual galaxies and absorbers for  $N_{\text{HI}} \gtrsim 10^{14.5} \text{ cm}^{-2}$  (see also Chen et al. 2005). At lower column densities ( $N_{\text{HI}} \lesssim 10^{14} \text{ cm}^{-2}$ ), there is no discernible trend (for Ly $\alpha$ -only or metal-line systems) which suggests these absorbers are predominantly associated with large-scale structures (e.g. intra-group material, filamentary structures).

If this qualitative picture is correct, one may comment on the luminosities of the galaxies hosting absorbers. Based on the systems with  $\rho_{min} < 100 h_{75}^{-1} \text{ kpc}$ , all of the galaxies are sub- $L_*$  although we note that the partial LLS at  $z = 0.16$  toward PKS0405–123 also shows an approximately  $2L_*$  galaxy at  $\rho < 100 h_{75}^{-1} \text{ kpc}$  (Spinrad et al. 1993). Of particular interest to examining the enrichment history of the IGM is to study the luminosity function of galaxies dominating such absorbers. We will address these issues in greater depth in a future paper summarizing our full set of galaxy surveys. Lastly, we comment that the average  $n_{gal}$  value may rise with  $N_{\text{HI}}$  but that there is apparently significant scatter in this crude measure of galactic environment.

## 8. DISCUSSION

We have discussed the reduction and analysis of archival *HST*/STIS and *FUSE* UV spectra of the low-redshift quasar PKS1302–102 ( $z_{QSO} = 0.2784$ ). We have

identified 95% of the potential Ly $\alpha$  features in STIS and  $> 80\%$  of the features in *FUSE* with  $> 4\sigma$  significance and  $\text{FWHM} = 20 \text{ km s}^{-1}$  and  $40 \text{ km s}^{-1}$ , respectively. We also performed a blind search for doublets without Ly $\alpha$  absorption; there were no such systems in the PKS1302–102 spectra. There are 23 Ly $\alpha$  systems; 14 are strong absorbers with  $\log N_{\text{HI}} > 14$ . Of those strong systems, seven are metal-line systems: four with C III only and three with C III and O VI, one of which is a tentative detection.

The unblocked redshift path length  $\Delta z$  for detecting Ly $\alpha$ , C III, or the O VI doublet was measured for regions where the  $W_r \geq 30 \text{ m\AA}$  absorption line(s) could be detected to  $> 3\sigma$  significance, excluding regions blocked by Galactic lines and within  $1500 \text{ km s}^{-1}$  of PKS1302–102 ( $z_{QSO} = 0.2784$ ). We quote the 68% confidence limits assuming Poisson statistics. With 23 Ly $\alpha$  absorbers and  $\Delta z = 0.251$ ,  $dN_{\text{Ly}\alpha}/dz = 92_{-10}^{+12}$ , which is lower but roughly consistent with other comparable published values,  $dN_{\text{Ly}\alpha}/dz \gtrsim 150$  (e.g., Penton et al. 2000; Richter et al. 2004; Sembach et al. 2004a). Similar to other published values (e.g., Richter et al. 2004; Prochaska et al. 2004; Danforth & Shull 2005), we derive  $dN_{\text{OVI}}/dz = 15_{-5}^{+8}$  for the three detections over  $\Delta z_{\text{OVI}} = 0.198$ . On the other hand, we measure  $dN_{\text{CIII}}/dz = 33_{-8}^{+11}$  from the six detections over  $\Delta z = 0.181$ . For their entire sample, DSRS06 measure  $dN_{\text{CIII}}/dz = 12_{-2}^{+3}$ . We agree with DSRS06 on the number of O VI and C III absorbers in the PKS1302–102 sightline; the difference in redshift density for these species is likely due to fluctuations between sightlines.

The four systems with only one metal line are modeled well by a single-phase absorber with  $[\text{M}/\text{H}] \approx -1$ , the currently favored value for  $N_{\text{HI}} > 10^{14} \text{ cm}^{-2}$  absorbers in the low- $z$  IGM (Prochaska et al. 2004; Danforth et al. 2006). The  $z_{abs} = 0.00442$ , 0.09400, and 0.19156 systems are likely photoionized media. The  $z_{abs} = 0.14529$  system may also be photoionized or collisionally ionized, assuming the Ly $\alpha$  width is due to all thermal broadening.

With only an upper limit on C III absorption, the  $z_{abs} = 0.06468$  O VI system could be reasonably modeled by either a photoionized or collisionally ionized medium. If the latter, the temperature is constrained to be  $T > 2.1 \times 10^5 \text{ K}$ , which could be a probe of the WHIM.

For the remaining two multiple metal-line systems, based primarily on kinematic arguments, they are better modeled by a multi-phase medium. In the case of the  $z_{abs} = 0.04321$  system, both C III and O VI are narrow but offset in by  $50 \text{ km s}^{-1}$ ; this system could be a two-phase photoionized medium with  $[\text{M}/\text{H}] \approx -0.75$ . On the other hand, O VI in the  $z_{abs} = 0.09487$  system is broad, implying a high temperature, while C III and Si III are narrow. Likely, the broad feature is due to a collisionally-ionized phase, and the narrow features are from a photoionized phase. The system has a relatively low metallicity,  $[\text{M}/\text{H}] \approx -2$ , for the photoionized gas.

The PKS1302–102 sight line has a galaxy survey complement. The survey gives compelling evidence that the metal-line absorption occurs in a diverse set of galactic environments. This includes a likely association with individual galactic halos ( $z_{abs} = 0.0948, 0.14253$ ), galaxy groups ( $z_{abs} = 0.0948, 0.192$ ) and relatively poor envi-

TABLE 9  
METAL ABSORBERS SUMMARY

$z_{abs}$	$\log N_{\text{HI}}$	$b_{\text{HI}}$	$\log N(\text{C}^{++})$	$\log N(\text{O}^{+5})$	Ion.	$\log U$	$[\text{M}/\text{H}]_{\text{phot}}$	$\log T_{\text{coll}}$	$[\text{M}/\text{H}]_{\text{coll}}$
0.00442	15.8	17	> 13.5	...	Photo	[-3.7, -1.7]	[-1.9, -1.6]	...	...
0.04226	15.07	22	13.7	14.5	Multi	[-3.5, -1.4]	[-0.9, -0.7]	> 5.4	-1.8
0.06468	14.47	26	< 13.1	13.8	???	> [C/O] - 1.5	[-1.2, -0.5]	> 5.3	[-1.2, -0.5]
0.09400	15.05	28	> 13.3	< 13.8	Photo	[-3.8, -0.9]	[-0.9, -0.6]	...	...
0.09487	16.87	31	> 13.9	14.1	Multi	[-3.5, -2.1]	[-2.1, -1.4]	> 5.3	-2.6
0.14529	15.37	57	14.2	< 14.1	Singl	[-4.1, [C/O]-1.3]	[-1.8, -0.5]	5.3	[-1.4, -1.2]
0.19156	15.27	23	13.1	< 14.1	Photo	[-4, [C/O]-1.3]	[-1.9, -0.7]	...	...

NOTE. — Ionization mechanism from relative abundances of measured species. In several cases, the mechanism is multi-phase or ambiguous. The bracketed values indicate the range of acceptable values.

ronments ( $z_{abs} = 0.06468$ ). The survey does not cover significant area at  $z_{abs} = 0.00442$ , the seventh metal-line system, but the sight line is known to pass through the Virgo cluster at this redshift.

In conclusion, none of the three O VI absorbers detected in the PKS1302–102 spectra definitively trace the warm-hot intergalactic medium, which is defined to be collisionally-ionized gas at  $T \approx 10^5$ – $10^7$  K. The system at  $z_{abs} = 0.06468$  may, though a firm conclusion is difficult to draw. In agreement with previous analysis (Prochaska et al. 2004; Richter et al. 2004), we find O VI absorption in a multi-phase medium. The two systems with at least O VI and C III must be multi-phase since C IV is not detected and the line profiles show different kinematic structure. However, these systems do not necessarily probe the WHIM, as seen in hydrodynamic simulations. The metal-line systems appear to probe the predominantly single-phase, photoionized in-

tergalactic medium at low redshift.

Based on observations made with the NASA-CNES-CSA *Far Ultraviolet Spectroscopic Explorer*. *FUSE* is operated for NASA by the Johns Hopkins University under NASA contract NAS5-32985.

Based on observations made with the NASA/ESA *Hubble Space Telescope* Space Telescope Imaging Spectrograph, obtained from the data archive at the Space Telescope Institute. STScI is operated by the association of Universities for Research in Astronomy, Inc. under the NASA contract NAS 5-26555.

The current study was funded by FUSE grant NAG5-12496.

*Facilities:* FUSE, HST (STIS), Las Campanas; Dupont

#### REFERENCES

- Blanton, M. R. et al. 2003, *ApJ*, 592, 819  
Bowen, D. V., Pettini, M., & Blades, J. C. 2002, *ApJ*, 580, 169  
Cen, R., & Fang, T. 2006, *ApJ*, 650, 573  
Cen, R., & Ostriker, J. P. 2006, *ApJ*, 650, 560  
Cen, R., Tripp, T. M., Ostriker, J. P., & Jenkins, E. B. 2001, *ApJ*, 559, L5  
Chen, H.-W., Lanzetta, K. M., & Webb, J. K. 2001a, *ApJ*, 556, 158  
Chen, H.-W., Lanzetta, K. M., Webb, J. K., & Barcons, X. 2001b, *ApJ*, 559, 654  
Chen, H.-W., & Prochaska, J. X. 2000, *ApJ*, 543, L9  
Chen, H.-W., Prochaska, J. X., Weiner, B. J., Mulchaey, J. S., & Williger, G. M. 2005, *ApJ*, 629, L25  
Corbett, E. A., Robinson, A., Axon, D. J., Young, S., & Hough, J. H. 1998, *MNRAS*, 296, 721  
Danforth, C. W., & Shull, J. M. 2005, *ApJ*, 624, 555  
Danforth, C. W., Shull, J. M., Rosenberg, J. L., & Stocke, J. T. 2006, *ApJ*, 640, 716  
Davé, R. et al. 2001, *ApJ*, 552, 473  
Fang, T., & Bryan, G. L. 2001, *ApJ*, 561, L31  
Ferland, G. J., Korista, K. T., Verner, D. A., Ferguson, J. W., Kingdon, J. B., & Verner, E. M. 1998, *PASP*, 110, 761  
Fukugita, M., & Peebles, P. J. E. 2004, *ApJ*, 616, 643  
Haardt, F., & Madau, P. 1996, *ApJ*, 461, 20  
Jenkins, E. B., Bowen, D. V., Tripp, T. M., & Sembach, K. R. 2005, *ApJ*, 623, 767  
Lanzetta, K. M., Bowen, D. V., Tytler, D., & Webb, J. K. 1995, *ApJ*, 442, 538  
Mobasher, B. 2002, *HST Data Handbook: Introduction to Reducing HST Data, Volume 1, Version 4.0 (User's Guide, Hubble Space Telescope, January 2002. Edited by Bahram Mobasher. Baltimore: Space Telescope Science Institute)*  
Moos, H. W. et al. 2000, *ApJ*, 538, L1  
Mulchaey, J. S., Davis, D. S., Mushotzky, R. F., & Burstein, D. 1996, *ApJ*, 456, 80  
Nicastro, F. et al. 2005, *ApJ*, 629, 700  
O'Meara, J. M., Burles, S., Prochaska, J. X., Prochter, G. E., Bernstein, R. A., & Burgess, K. M. 2006, *ApJ*, 649, L61  
Penton, S. V., Shull, J. M., & Stocke, J. T. 2000, *ApJ*, 544, 150  
Penton, S. V., Stocke, J. T., & Shull, J. M. 2002, *ApJ*, 565, 720  
— 2004, *ApJS*, 152, 29  
Prochaska, J. X., Chen, H.-W., Howk, J. C., Weiner, B. J., & Mulchaey, J. 2004, *ApJ*, 617, 718  
Prochaska, J. X., Weiner, B. J., Chen, H.-W., & Mulchaey, J. S. 2006, *ApJ*, 643, 680  
Richter, P., Fang, T., & Bryan, G. L. 2006, *A&A*, 451, 767  
Richter, P., Savage, B. D., Tripp, T. M., & Sembach, K. R. 2004, *ApJS*, 153, 165  
Sahnow, D. J. et al. 2000, *ApJ*, 538, L7  
Savage, B. D., & Sembach, K. R. 1991, *ApJ*, 379, 245  
Sembach, K. R., Tripp, T. M., Savage, B. D., & Richter, P. 2004a, *ApJS*, 155, 351  
— 2004b, *ApJS*, 155, 351  
Shull, J. M., Tumlinson, J., & Giroux, M. L. 2003, *ApJ*, 594, L107  
Simcoe, R. A., Sargent, W. L. W., & Rauch, M. 2002, *ApJ*, 578, 737  
Spergel, D. N. et al. 2006, *ArXiv Astrophysics e-prints*  
Spinrad, H. et al. 1993, *AJ*, 106, 1  
Stocke, J. T., Keeney, B. A., McLin, K. M., Rosenberg, J. L., Weymann, R. J., & Giroux, M. L. 2004, *ApJ*, 609, 94  
Stocke, J. T., Penton, S. V., Danforth, C. W., Shull, J. M., Tumlinson, J., & McLin, K. M. 2006, *ApJ*, 641, 217  
Tripp, T. M., Aracil, B., Bowen, D. V., & Jenkins, E. B. 2006a, *ApJ*, 643, L77  
Tripp, T. M., Bowen, D. V., Sembach, K. R., Jenkins, E. B., Savage, B. D., & Richter, P. 2006b, in *Astronomical Society of the Pacific Conference Series*, ed. G. Sonneborn, H. W. Moos, & B.-G. Andersson, 341–+  
Tripp, T. M., & Savage, B. D. 2000, *ApJ*, 542, 42  
Tripp, T. M., Savage, B. D., & Jenkins, E. B. 2000, *ApJ*, 534, L1  
Wakker, B. P. 2006, *ApJS*, 163, 282  
Wakker, B. P. et al. 2003, *ApJS*, 146, 1  
Wang, Q. D. et al. 2005, *ApJ*, 635, 386  
Williams, R. J., Mathur, S., & Nicastro, F. 2006, *ApJ*, 645, 179

TABLE 10  
SUMMARY OF GALAXIES NEIGHBORING ABSORPTION SYSTEMS

ID	$z_{gal}$	$R$	$L$ ( $L^*$ )	$\delta v$ ( $\text{km s}^{-1}$ )	$\rho$ ( $h_{75}^{-1} \text{kpc}$ )	$E_C$	$L_C$
$z_{abs} = 0.04226, \log N_{\text{HI}} = 15.1, \log N(\text{O VI}) = 14.5$							
2447	0.04256	14.1	2.71	87	212	0.41	0.57
2226	0.04196	16.3	0.35	-88	294	-0.17	0.42
$z_{abs} = 0.06468, \log N_{\text{HI}} = 14.5, \log N(\text{O VI}) = 13.8$							
1576	0.06468	19.4	0.05	0	337	0.91	0.10
1712	0.06523	15.4	1.95	155	485	0.97	-0.04
$z_{abs} = 0.09487, \log N_{\text{HI}} = 16.9, \log N(\text{O VI}) = 14.0^a$							
2033	0.09358	18.8	0.19	-352 (-115)	64	0.98	-0.03
2415	0.09328	19.2	0.12	-433 (-196)	292	0.99	-0.04
2435	0.09393	15.2	5.21	-257 (-20)	331	0.97	-0.19
2391	0.09331	18.1	0.33	-426 (-189)	362	0.61	0.44
2790	0.09531	19.3	0.12	122 (359)	528	0.87	0.03
2685	0.09258	17.3	0.73	-625 (-388)	575	0.81	-0.03
2867	0.09523	16.9	1.10	99 (337)	685	0.85	0.16
2682	0.09442	16.9	1.10	-123 (114)	687	0.91	0.22
1711	0.09332	18.5	0.23	-422 (-185)	703	0.13	0.93
2193	0.09402	16.2	1.97	-233 (4)	797	0.85	0.29
$z_{abs} = 0.09897, \log N_{\text{HI}} = 14.2$							
2790	0.09531	19.3	0.12	-997	528	0.87	0.03
$z_{abs} = 0.14529, \log N_{\text{HI}} = 15.3, \log N(\text{O VI}) < 14.2$							
1909	0.14530	18.9	0.42	2	80	0.09	0.82
1708	0.14292	17.3	1.87	-621	561	0.97	0.03
1920	0.14536	17.9	1.13	17	951	-0.08	0.66
1921	0.14500	17.1	2.26	-77	964	0.42	0.57
768	0.14202	17.6	1.37	-857	1374	0.86	0.31
1564	0.14685	17.2	2.06	409	1502	0.78	0.36
$z_{abs} = 0.19156, \log N_{\text{HI}} = 15.3, \log N(\text{O VI}) < 14.1$							
1926	0.19171	18.9	0.77	37	206	0.99	-0.01
2051	0.19239	18.3	1.32	208	433	0.99	-0.08
2232	0.19296	19.0	0.73	353	465	-0.16	0.70
1664	0.19361	18.0	1.91	515	520	0.99	-0.03
$z_{abs} = 0.19242, \log N_{\text{HI}} = 14.1$							
1926	0.19171	18.9	0.77	-180	206	0.99	-0.01
2051	0.19239	18.3	1.32	-9	433	0.99	-0.08
2232	0.19296	19.0	0.73	136	465	-0.16	0.70
1664	0.19361	18.0	1.91	297	520	0.99	-0.03
$z_{abs} = 0.22449, \log N_{\text{HI}} = 14.1$							
1821	0.22557	19.4	0.74	264	416	0.93	0.25
1253	0.22690	17.7	3.63	591	1132	1.00	-0.07
3074	0.22772	18.9	1.15	791	1542	0.87	0.29
3152	0.22584	18.0	2.51	329	1653	0.92	0.23
3208	0.22687	17.8	3.08	583	1699	0.99	-0.05
$z_{abs} = 0.22552, \log N_{\text{HI}} = 14.0$							
1821	0.22557	19.4	0.74	12	416	0.93	0.25
1253	0.22690	17.7	3.63	339	1132	1.00	-0.07
3074	0.22772	18.9	1.15	539	1542	0.87	0.29
3152	0.22584	18.0	2.51	77	1653	0.92	0.23
3208	0.22687	17.8	3.08	331	1699	0.99	-0.05
$z_{abs} = 0.24877, \log N_{\text{HI}} = 14.2$							
2573	0.25012	19.0	1.30	323	2165	0.99	-0.11
3314	0.24942	17.8	3.99	155	2214	0.68	0.31
2510	0.24852	18.0	3.23	-62	2253	1.00	-0.04
2378	0.24786	18.7	1.65	-218	2367	0.67	0.44
2726	0.24873	18.3	2.38	-10	2445	0.99	-0.11
2832	0.24892	18.1	2.96	35	2522	0.98	-0.12
2973	0.24882	19.1	1.19	12	2599	0.98	-0.12
179	0.24866	18.0	3.38	-27	2996	0.94	0.15

TABLE 10 — *Continued*

ID	$z_{gal}$	$R$	$L$ ( $L^*$ )	$\delta v$ ( $\text{km s}^{-1}$ )	$\rho$ ( $h_{75}^{-1}$ kpc)	$E_C$	$L_C$
$z_{abs} = 0.25216, \log N_{\text{HI}} = 14.8$							
1413	0.25398	19.0	1.30	438	1707	0.72	0.45
2573	0.25012	19.0	1.30	-487	2165	0.99	-0.11
3314	0.24942	17.8	3.99	-655	2214	0.68	0.31
2510	0.24852	18.0	3.23	-871	2253	1.00	-0.04
2726	0.24873	18.3	2.38	-819	2445	0.99	-0.11
2832	0.24892	18.1	2.96	-775	2522	0.98	-0.12
2973	0.24882	19.1	1.19	-798	2599	0.98	-0.12
179	0.24866	18.0	3.38	-836	2996	0.94	0.15

NOTE. — The galaxy summary is restricted to those galaxies within  $1000 \text{ km s}^{-1}$  of the absorption system. The impact parameter refers to physical separation, not comoving.

<sup>a</sup> ( $z_{abs} = 0.09400, \log N_{\text{HI}} = 15.1, \log N(\text{O VI}) < 13.8$ )